

# SEAR: Simple and Efficient Adaptation of Visual Geometric Transformers for RGB+Thermal 3D Reconstruction

Vsevolod Skorokhodov<sup>1</sup>, Chenghao Xu<sup>2</sup>, Shuo Sun<sup>3</sup>, Olga Fink<sup>2</sup>, and Malcolm Mielle<sup>1</sup>

<sup>1</sup> Schindler EPFL Lab, Lausanne, Switzerland

<sup>2</sup> EPFL, Lausanne, Switzerland

<sup>3</sup> Örebro University, Örebro, Sweden

**Abstract.** Foundational feed-forward visual geometry models enable accurate and efficient camera pose estimation and scene reconstruction by learning strong scene priors from massive RGB datasets. However, their effectiveness drops when applied to mixed sensing modalities, such as RGB-thermal (RGB-T) images. We observe that while a visual geometry grounded transformer pretrained on RGB data generalizes well to thermal-only reconstruction, it struggles to align RGB and thermal modalities when processed jointly. To address this, we propose SEAR, a simple yet efficient fine-tuning strategy that adapts a pretrained geometry transformer to multimodal RGB-T inputs. Despite being trained on a relatively small RGB-T dataset, our approach significantly outperforms state-of-the-art methods for 3D reconstruction and camera pose estimation, achieving significant improvements over all metrics (e.g., over 29% in AUC@30) and delivering higher detail and consistency between modalities with negligible overhead in inference time compared to the original pretrained model. Notably, SEAR enables reliable multimodal pose estimation and reconstruction even under challenging conditions, such as low lighting and dense smoke. We validate our architecture through extensive ablation studies, demonstrating how the model aligns both modalities. Additionally, we introduce a new dataset featuring RGB and thermal sequences captured at different times, viewpoints, and illumination conditions, providing a robust benchmark for future work in multimodal 3D scene reconstruction. Code and models are publicly available at <https://www.github.com/Schindler-EPFL-Lab/SEAR>.

**Keywords:** Multimodal Pose Estimation · Thermal imagery · Feed-Forward Neural Network

## 1 Introduction

Recent work introduced large-scale 3D geometric foundation models as adaptable solutions for in-the-wild 3D vision tasks (e.g., reconstruction, pose estimation,

novel view synthesis). Unlike traditional photogrammetry pipelines—which depend on feature matching and iterative optimization—these models use transformers to predict camera poses and scene structure from sparse RGB inputs in a single feed-forward pass [39]. Pretrained on diverse datasets, they achieve strong cross-scene generalization, addressing classical limitations like computational inefficiency and sensitivity to image quality and environmental conditions. Despite these advances, current geometric foundation models rely solely on RGB inputs, limiting their robustness in real-world scenarios where complementary modalities are needed. E.g., thermal cameras capture long-wave infrared radiation, enabling applications such as low-light reconstruction [44], thermal simulation [2], and infrastructure inspection [9].

When applying a pretrained feed-forward model (e.g., VGGT [39]) to mixed RGB-thermal inputs, we observe independent reconstructions that fail to align into a coherent 3D representation (see Fig. 3). This indicates that while pretrained models encode strong geometric priors, they lack explicit cross-modal consistency for pose estimation and reconstruction. Prior works have mostly addressed this issue via either synchronous data collection [9, 2, 21, 20], or post-hoc alignment [36]. In simultaneous capture, using paired images from both modalities, a “strong” modality (e.g., RGB) infers poses for a “weaker” one (e.g., thermal) using classical pipelines like COLMAP [31]. In practice, synchronous captures necessitate complex or expensive sensor setups, and real-world data is often asynchronous (e.g., thermal imagery at sunrise for steady-state facades [42] vs. RGB at daytime for visual clarity [9].) Post-hoc alignment methods, on the other hand, use cross-modal feature matching to align poses/images using specialized descriptors; those methods are thus sensitive to image, feature, and match quality, leading to lower robustness. Thus, estimating consistent multimodal camera poses and 3D scene reconstruction in realistic scenarios is still a challenge.

In this work, we address camera pose estimation and scene reconstruction from unpaired RGB and thermal (RGB-T) images. Our key insight is that, since VGGT performs well on each modality independently when processed jointly but lacks geometric consistency, large-scale multimodal retraining should be unnecessary. Instead, a pretrained model can be adapted with minimal parameter updates to bridge the modality gap. Our contributions are threefold:

- We propose SEAR, a lightweight fine-tuning strategy for cross-modal pose estimation and 3D reconstruction, based on LoRA-based adapters, modality-specific tokens, and a specific batching strategy. Our method requires fewer than 5% of the original model’s parameters and preserves the inference speed of the base model.
- We show that SEAR only requires a modest multimodal dataset for tuning ( $\sim 15,000$  pairs of RGB and thermal images), making it practical for real-world applications where collecting large multimodal dataset is challenging.
- We present a new dataset comprising 9 scenes ( $\sim 2,000$  images) with distinct RGB/thermal trajectories captured under varying illumination and viewpoints. This dataset provides a new benchmark for evaluating RGB-T cross-spatial multimodal reconstruction in challenging conditions.

- Through extensive experiments, we demonstrate large improvements against six state-of-the-art baselines, in pose estimation (e.g., +30% AUC@30) and point cloud reconstruction metrics. Complementary ablation studies further support our key design choices.

## 2 Related Works

Multimodal sensing enables applications beyond RGB-only. RGB-T imaging enables low-light scene mapping and non-invasive infrastructure inspection (e.g., detecting thermal defects via finite element analysis [2]). Though NeRF [9, 19] and Gaussian Splatting [20, 23] have been extended to RGB-T data, they depend on known camera poses—typically estimated via SfM [31] or single-modality feed-forward networks, which fail for cross-modal datasets (see Fig. 3). Thus, most prior work [9, 2, 20] assumes paired multimodal datasets, using RGB to obtain pose estimates for other modalities.

To estimate camera poses and scene reconstruction, traditional 3D reconstruction relies on iterative optimization (e.g., SfM [31] or SLAM [34]), on the detection of salient features (e.g., ORB [26]), and on computationally expensive matching algorithms (e.g., PnP [43] or RANSAC [6]). While these methods can struggle with robustness and generalization, recent feed-forward models use transformers to predict camera poses and 3D geometry in a single pass [40, 17, 39], achieving strong zero-shot generalization. However, these methods are trained on unimodal inputs (e.g., RGB) and their use for applications where multimodal data (e.g., thermal, depth) is necessary for robustness remains limited.

Retraining large models for multimodal tasks is computationally prohibitive for most machine learning practitioners. Furthermore, RGB and thermal datasets for scene reconstruction are scarce (e.g., ThermoNeRF’s 20 scenes [9]), with larger RGB+thermal datasets focusing on segmentation/navigation. Parameter-efficient fine-tuning (PEFT) methods address this by reducing the number of trainable parameters while preserving performance.

Key approaches include Adapter Layers [12] (lightweight modules inserted between transformer layers), Prompt Tuning [18] (optimizes continuous prompts in embedding space), and Low-Rank Adaptation (LoRA) [13] (decomposes weight updates into low-rank matrices). While PEFT has been applied in NLP [14] and visual segmentation [24], existing work focuses on task specialization—not modality expansion. No prior work explores PEFT to adapt pretrained 3D geometric models to multimodal reconstruction. By bridging this gap, our work lays the foundation for resource-efficient, generalizable multimodal reconstruction.

## 3 Preliminaries: VGGT

VGGT [39] is a transformer-based model able to estimate, from a sequence of  $N$  RGB images observing a 3D scene, the intrinsic and extrinsic camera parameters, a depth map, a point map, and a grid of  $C$ -dimensional features for point tracking. DINOv2 [27] performs feature extraction under the hood, producing a sequence of

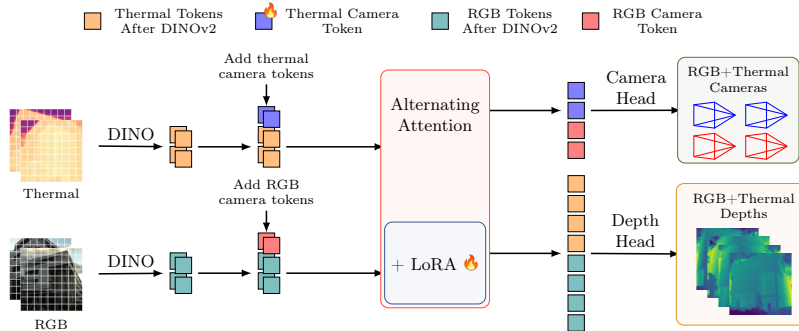


**Fig. 1:** SEAR architecture. RGB and thermal images are first tokenized using DINOv2. For each modality, camera-specific tokens are concatenated with the corresponding DINO tokens. The combined tokens are then processed by an Alternating Attention (AA) module with LoRA adapters. Finally, the refined tokens are passed to separate prediction heads for camera parameter estimation and depth estimation. Trainable parameters are highlighted with a flame symbol.

tokens for each input frame. After that, a learnable *camera token* is concatenated to each set of tokens of each frame. The resulting token sequence is processed by 24 self-attention blocks, with alternating (frame-wise and global) attention (AA) blocks. The tokens from the last layer are passed to the camera parameters prediction head, while intermediate tokens from layers 4, 11, 17, and 23 are concatenated and passed to depth, point map, and tracking prediction heads. For more details, refer to the original paper [39].

## 4 Methodology

While VGGT can be used to estimate RGB or thermal 3D scenes, estimated RGB-T scenes often result in two disjoint reconstructions (one per modality), misaligned in pose and scale (see Fig. 3). We hypothesize that this knowledge gap can be closed by fine-tuning the pretrained model, drastically reducing computational cost compared to retraining.

We introduce a framework (see Fig. 1) to adapt VGGT [39] for joint estimation of RGB and thermal intrinsic/extrinsic camera parameters and depth maps. We introduce three innovations: 1) Lightweight LoRA adapters in the AA module to bridge the domain gap between RGB and thermal inputs (Sec. 4.1). 2) A learnable thermal camera token to capture modality-specific features (Sec. 4.2). 3) A batching strategy designed to prevent the model from relying on RGB-T image correspondences (Sec. 4.4). Our method enables RGB-T scene reconstruction and camera pose estimation with negligible memory and inference overhead.

### 4.1 LoRA Integration

We fine-tune the RGB-pretrained VGGT model using LoRA to adapt it for mixed RGB+thermal inputs. LoRA modules are integrated into all linear and multi-head attention layers of the alternating-attention (AA) module. This approach preserves the model’s pretrained RGB knowledge, since the original weights are frozen; the original RGB and thermal data processing is left unchanged, pushing the model to focus on alignment between the modalities to reduce the loss during training. The features produced by the AA module are then processed by the prediction heads to estimate camera parameters and depth maps with their uncertainties. The adapter follows the default LoRA initialization scheme [13].

### 4.2 Thermal Camera Token

The original VGGT model uses DINOv2 [27] as a tokenizer and visual feature extractor for RGB images. For each frame, a camera token is appended to the image tokens, and the sequence is processed by the AA module. Prior work [5] has shown that while DINOv2 is able to extract meaningful thermal features without retraining, the feature distributions of the two modalities differ. Hence, we use DINOv2 as a tokenizer for both modalities, and, to align both modalities’ feature spaces before the AA module, we introduce two learnable thermal camera tokens—a counterpart to the two original VGGT camera tokens (now termed the RGB camera token). These tokens encode the intrinsic/extrinsic features for thermal frames—the first token is for the first frame of the sequence, while the other is for all subsequent frames. RGB and thermal images are independently tokenized using DINOv2 before the RGB camera token and the learnable thermal camera token are respectively appended to the RGB and thermal tokens. Then, the augmented sequences are fed into the AA module. By assigning distinct camera tokens to each modality, the model learns modality-specific representations. Since these tokens are used in both frame-wise and global interactions in the AA module, they enable differentiated processing of RGB and thermal inputs.

To preserve the pretrained model’s behavior during early tuning, we initialize the thermal camera token with the RGB camera token’s weights.

### 4.3 Optimization

We optimize our model using the loss functions from VGGT, formulated as a multitask loss:

$$\mathcal{L} = \lambda_{camera}\mathcal{L}_{camera} + \mathcal{L}_{depth}. \quad (1)$$

Where  $\mathcal{L}_{camera}$  is the Huber loss for camera poses estimation,  $\mathcal{L}_{depth}$  is an uncertainty-aware loss for depth prediction, and  $\lambda_{camera}$  is a weighting coefficient set to 5.0, as in the original VGGT model.

#### 4.4 Data Pre-processing and Batching

We apply asymmetric augmentation pipelines for RGB and thermal inputs. For both RGB and thermal images, we apply random cropping, random aspect ratio adjustments (uniformly sampled from  $[0.33, 1.0]$ ), Gaussian noise, Gaussian blur, and random sharpness adjustments. For RGB images, we further apply color jittering and grayscale conversion. For thermal images, we apply random linear transformations of pixel intensities followed by random exponential scaling of pixel values with degree sampled uniformly in  $[1/1.5, 1.5]$ . Additionally, we apply random  $90^\circ$  rotations to both RGB and thermal images.

To ensure generalization to inputs of varying ratios and sizes, we construct batches of independent RGB and thermal images—i.e., without shared camera poses—sampled from a single RGB+thermal scene. This constraint prevents the model from relying on trivial RGB-thermal correspondences during training, instead forcing it to learn inter-modal relationships across viewpoints. The ratio of thermal to RGB images  $\tau$  within each batch is randomly sampled from a uniform distribution  $U(0, 1)$ , enabling the model to process arbitrary combinations of RGB and thermal inputs.

## 5 Datasets

### 5.1 Novel Challenging Cross-Spatial RGB-T Dataset

We introduce a novel multimodal RGB+thermal dataset of 1,890 paired images across nine diverse scenes, captured using a FLIR One Pro LT [35]. The dataset includes residential and outdoor environments (e.g., buildings, structures) as well as objects (e.g., metallic items, a telescope), which are visualized in Fig. 2. To assess cross-spatial reconstruction, each scene includes paired RGB-thermal images captured along two distinct trajectories. The dataset is publicly available [33].

The dataset consists of two subsets, differentiated by trajectory characteristics and environmental conditions. The first subset consists of six scenes (upper section of Fig. 2) captured under consistent, well-lit conditions (e.g., daytime or artificially illuminated indoor settings). Trajectories are non-intersecting, simulating independent data collection by separate sensors. Ground-truth poses are estimated using VGGT on all RGB images from both trajectories. The second subset (bottom section of Fig. 2) consists of three scenes captured under varying lighting (i.e., outdoor scenes spanning day/night). Since half of all scenes are low-illumination, RGB-based camera pose estimation is unreliable. Given the high uncertainty of pose estimation from thermal images, this subset is used for qualitative assessment due to the lack of reliable ground-truth.

### 5.2 Publicly Available Datasets

Despite the scarcity of RGB-thermal datasets with ground-truth poses, we show that fine-tuning our model requires only limited real-world data. Our training set includes 66 scenes (around 15,000 RGB+thermal image pairs), aggregated

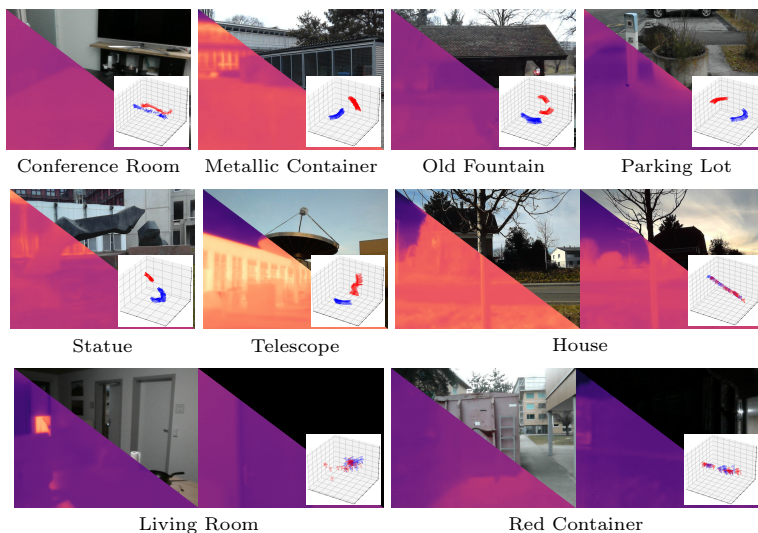


**Fig. 2:** The SEAR dataset includes 9 scenes, each with paired RGB-thermal images captured along two distinct trajectories. Ground-truth poses (red/blue for each trajectory) are estimated via VGGT on all RGB images. The top 6 scenes feature trajectories under similar lighting, while the bottom 3 have large lighting variations (some RGB images are near fully black).

from five publicly available datasets and randomly split into 48 training and 18 evaluation scenes: ThermoScenes [9] 15(train)/5(val), ThermalNeRF [21] 8/2, ThermalGaussian [20] 11/3, ThermalMix [28] 4/2, and the Radar Forest (RF) Dataset<sup>4</sup> 9/6. Scene names per split are listed in the Supplementary Material. We exclude datasets not designed for scene reconstruction (e.g., autonomous driving datasets like [16, 32]).

For ThermoScenes, ThermalGaussian, and ThermalMix, RGB and thermal images are paired with identical extrinsics. We derive ground-truth extrinsics, intrinsics, and depth from VGGT reconstructions on RGB images, then transfer these to corresponding thermal frames. Since our goal is cross-modal reconstruction from unpaired data (not improving VGGT’s pose estimation), using VGGT-derived RGB poses as ground truth does not bias validation. In ThermalNeRF [21], RGB and thermal images are paired via a known rigid transformation. We estimate RGB extrinsics using VGGT and derive thermal extrinsics by applying the rigid transform. Thermal depth maps are generated by projecting RGB depth estimates into 3D world points and reprojecting them onto the thermal frame. The RF dataset includes high-precision camera poses captured via a motion capture system and sparse LiDAR point clouds—both serving as ground truth in evaluation, eliminating the need for ground truth estimation

<sup>4</sup> a yet-to-be-published extension of [https://github.com/RNP-lab/viking\\_hill\\_radar\\_lidar\\_camera\\_dataset](https://github.com/RNP-lab/viking_hill_radar_lidar_camera_dataset)

using VGGT. We generate depth maps by projecting LiDAR points into the camera frame using the provided extrinsics and intrinsics.

### 5.3 Data Split of Evaluation Scenes

Validation uses a fixed thermal ratio of  $\tau = 0.5$  (to avoid modality imbalance) and a batch size equal to the total number of frames per scene. As for training, we ensure that no RGB and thermal images in a batch share the same pose; given paired images, each scene is evaluated twice by swapping RGB and thermal image selections. This eliminates possible selection bias (since both runs are complementary to each other) and yields 36 evaluation cases (18 scenes  $\times$  2).

For evaluation on SEAR dataset, we use the dataset’s split into two non-overlapping trajectories, pairing thermal images from one with RGB from the other. Each of the 6 scenes is evaluated twice (once per modality-trajectory pair), yielding 12 evaluation cases. We additionally include SmokeSeer [15], which provides two RGB-thermal drone scenes (both with and without dense smoke) but lacks ground-truth poses. We use SmokeSeer for qualitative evaluation only since, unlike other datasets, VGGT-based pose estimation fails here due to high uncertainty on smoke-occluded RGB frames.

## 6 Experiments

### 6.1 Implementation Details

Our model’s trained weights and implementation are available online<sup>5</sup>. We use the VGGT checkpoint from HuggingFace<sup>6</sup>. Training uses bf-16 mixed precision, AdamW optimizer with learning rate of  $5 \cdot 10^{-5}$  and weight decay of  $10^{-2}$ , linear warmup scheduling (first 10% of epochs, LR from 0.0 to  $5 \cdot 10^{-5}$ ). We train the model for 100 epochs with a batch size of 24 (around 2 days on a single A100). To improve scalability and generalization to arbitrary input sizes, we follow VGGT’s approach and partition the 24 frames of each batch into  $N \in \{1, 2, 3, 4, 6, 12\}$  equal-length sequences. To reduce variations due to known numerical instabilities [45], we fine-tune 13 models with different seeds and report their average metrics.

To demonstrate that bridging the multimodal knowledge gap requires only minimal fine-tuning, the LoRA rank used is  $r = 64$  and the scaling factor  $\alpha = 128$ , yielding  $\sim 50$ M trainable parameters—less than 5% of the original model’s size. Since, as established in the original LoRA paper, tuning  $\alpha$  is equivalent to adjusting the learning rate, we fix  $\alpha$  and optimize the learning rate empirically across all scenes in the ThermoScenes dataset.

### 6.2 Baselines and Metrics

We benchmark against traditional SfM (COLMAP [31] with SuperPoint + SuperGlue [30]) and deep-learning based models (DUSt3R [40], MAST3R [17] and

<sup>5</sup> <https://www.github.com/Schindler-EPFL-Lab/SEAR>

<sup>6</sup> <https://huggingface.co/facebook/VGGT-1B>

pretrained VGGT). Since these methods lack multimodal support, we input RGB/thermal images as a single modality. We also benchmark against hybrid approaches mixing feature matching and deep learning. We use  $\text{MA}_{\text{ELOFTR}}$  (ELOFTR [41] trained with MatchAnything [10]) and  $\text{MINIMA}_{\text{ROMA}}$  (RoMA [3] trained with MINIMA [29]) to establish RGB-thermal correspondences, followed by DIM [25] for 3D reconstruction and pose estimation. We use publicly available implementations and official pretrained weights for all baselines and use identical data splits and computational resources (one A100 GPU) for all methods. Classical approaches are evaluated using their default parameters.

Following VGGT [39], we evaluate the methods using the  $\text{RRA@30}$  and  $\text{RTA@30}$  (percentages of image pairs with relative rotation/translation errors  $< 30^\circ$ ) and  $\text{AUC@30}$  (area under the accuracy-threshold curve of the maximum values between RRA and RTA with thresholds  $[5.0, 15.0, 30.0]^\circ$ ). We also report the processed frames per second (FPS) and registration rate (Reg.) [4] (percentage of successfully registered images). We compute the quality metrics on registered cameras only, excluding images without predicted poses. When LiDAR data is available, we report point cloud completeness (PCC) (the mean nearest-neighbor distance from reconstruction to LiDAR) and point cloud accuracy (PCA) (the mean nearest-neighbor distance from LiDAR to reconstruction). We also report the Chamfer distance, i.e., the average of PCC and PCA. To compute these metrics, we align estimated and ground-truth camera poses using Umeyama alignment [37], back-project estimated depth maps, and calculate the metrics between estimated and ground-truth point clouds. To mitigate bias toward methods that perform well on only a subset of scenes, we report the metrics over the errors across all datasets/scenes (for scene-agnostic evaluation) in Tab. 1.

### 6.3 Multimodal Camera Pose Estimation

Our method significantly outperforms all baselines (see Tab. 1) while maintaining a high registration rate. E.g., we achieve an  $\text{AUC@30}$  of 70.0 on the Public Datasets and of 62.8 on our SEAR dataset, compared to 41.0/48.2 for  $\text{MINIMA}_{\text{ROMA}}$ , the method with the second-highest performance and a strong registration rate—though COLMAP achieves better metrics, its low registration rate artificially boosts those results. Non-multimodal approaches (COLMAP, DUST3R, MAST3R, VGGT) fail on thermal images due to the lack of discriminative features for cross-modal alignment, often producing disjoint reconstructions (see Fig. 3)—e.g., COLMAP only registers frames of only one modality.  $\text{MA}_{\text{ELOFTR}}$  produces sparse matches leading to low registration rates and poor 3D reconstructions. Furthermore, our method is  $200\times$  faster (10.46 FPS vs.  $\text{MINIMA}_{\text{ROMA}}$ 's 0.05 FPS), nearly matching VGGT's speed (9.94 FPS vs. 10.46 FPS). Unlike other methods, SEAR achieves consistent RGB-T scene reconstruction.

### 6.4 Multimodal Point Cloud Reconstruction

As shown in Tab. 1, SEAR achieves the highest point cloud metrics: PCC of 0.06, PCA of 0.47, and Chamfer distance of 0.27. The next-best method, MAST3R,

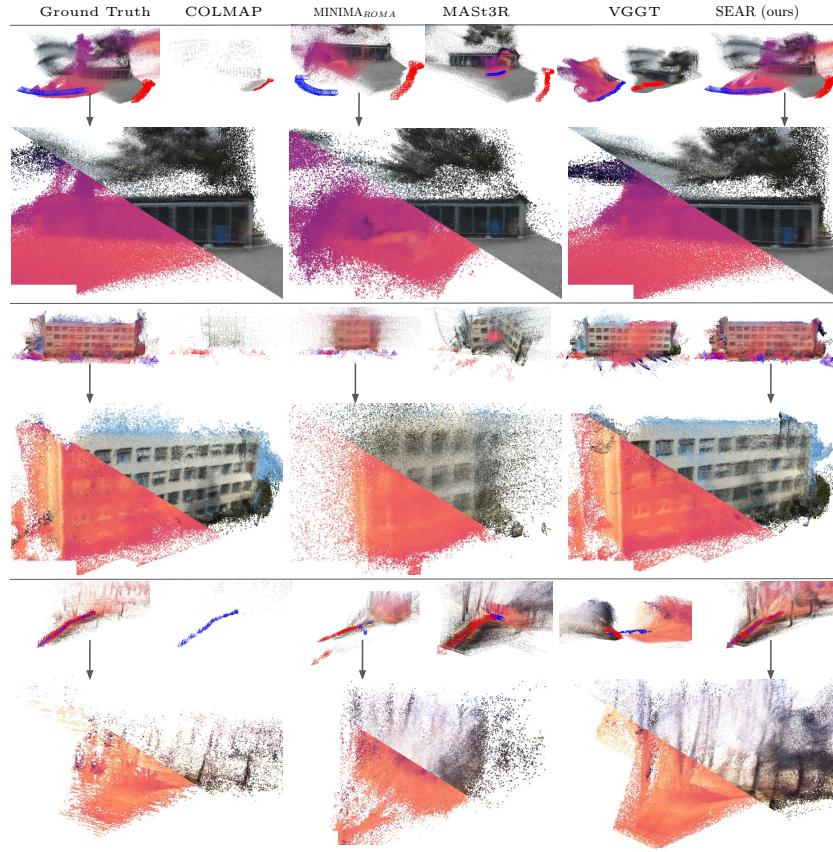


**Fig. 3:** Qualitative results comparing RGB/thermal reconstructions (camera poses in red/blue); we show results for 4 methods at rows 1, 3, and 5, and zoom in on more interesting reconstruction details in rows 2, 4, and 6. Our method (SEAR) achieves higher accuracy, consistency, and level of detail than other methods.

only has a PCC of 0.27, PCA of 0.66, and Chamfer distance of 0.46, while COLMAP+SPSG produces single-modality sparse point clouds. For hybrid methods, the quality of 3D reconstructions is dependent on the 2D-2D correspondences’ quality and density;  $MA_{ELOFTR}$  only detected a small number of correspondences, leading to low metrics.  $MINIMA_{ROMA}$  finds more correspondences but their uncertainty results in low quality reconstructions—its Chamfer distance is only 1.03 compared to 0.26 for our method.

While point cloud metrics are only calculated against scenes with LiDAR ground truth, Fig. 3 provides additional qualitative comparisons across diverse scenes. DUST3R, MAST3R, and VGGT frequently generate disjoint 3D representations for each modality, exhibiting inconsistencies in both scale and spatial alignment between modalities.  $MINIMA_{ROMA}$  reconstructs less detailed point clouds than our method, which reconstructs consistent multimodal point clouds.

**Table 1:** Quantitative comparison of 3D reconstruction methods for all datasets. Metrics include **AUC**, **RRA**, and **RTA @30** (higher is better,  $\uparrow$ ), point cloud accuracy **PCA**, point cloud completeness **PCC**, **Chamfer** distance (lower is better,  $\downarrow$ ), registration rate **Reg.** (higher is better,  $\uparrow$ ), and frames per second **FPS** (higher is better,  $\uparrow$ ). Best and second-best results are highlighted in blue and light blue, respectively.

Method	Public Datasets								SEAR Dataset				
	AUC $\uparrow$	RRA $\uparrow$	RTA $\uparrow$	PCA $\downarrow$	PCC $\downarrow$	Chamfer $\downarrow$	Reg (%) $\uparrow$	FPS $\uparrow$	AUC $\uparrow$	RRA $\uparrow$	RTA $\uparrow$	Reg (%) $\uparrow$	FPS $\uparrow$
COLMAP +SPSG	57.6	82.5	74.6	1.64	1.20	1.42	44.7	0.44	74.4	99.9	95.9	27.9	0.66
MA <sub>ELOFTR</sub>	13.1	70.1	41.2	0.49	5.16	2.82	21.8	0.21	15.9	73.7	53.1	37.3	0.17
MINIMA <sub>ROMA</sub>	41.0	68.3	63.0	0.97	1.09	1.03	98.7	0.05	48.2	65.9	68.9	100.0	0.04
DUST3R	18.9	45.9	42.1	0.72	4.72	2.72	100.0	0.66	18.7	51.0	39.2	100.0	0.67
MASt3R	30.8	69.7	55.8	0.66	0.27	0.46	100.0	0.24	39.1	54.9	56.3	100.0	0.25
VGGT	22.9	50.7	48.5	1.22	2.60	1.91	100.0	10.46	23.3	50.5	56.4	100.0	10.51
SEAR	70.0	90.6	87.6	0.47	0.06	0.27	100.0	9.94	62.8	83.7	84.2	100.0	10.22

## 6.5 Qualitative Evaluation

We perform qualitative evaluation on SmokeSeer [15] and the subset of our new dataset with varying lighting conditions (see Fig. 4). Under challenging conditions, SEAR estimates well-aligned 3D camera poses across both RGB and thermal modalities, reconstructing the scenes with details, and demonstrating robust performance under challenging conditions (when both modalities are captured at different times or smoke is occluding the scene). In comparison, MASt3R and MINIMA<sub>ROMA</sub> misalign RGB/thermal reconstructions (rotated, improperly scaled thermal point cloud, with camera pose not consistent between modalities). On the other hand, VGGT sometimes achieves partial alignment (e.g., top image of Fig. 4), but the results are inconsistent and noisy (e.g., alignments are wrong on scenes from our new dataset), especially in the thermal domain. Additional qualitative results are provided in the Supplementary Material.

## 6.6 Varying thermal to RGB ratio

Prior experiments assumed a balanced RGB-thermal ratio ( $\tau = 0.5$ ). To evaluate robustness to unequal ratios, we vary  $\tau \in [0, 1]$  and report camera pose estimation in Fig. 5. For each  $\tau$ , we perform three random inferences per scene with randomly selected non-corresponding RGB-thermal pairs to reduce statistical variance. Fig. 5 shows a slow but constant performance decrease as  $\tau$  increases, with a slight recovery after  $\tau \approx 0.75$ .

We hypothesize that the metrics decrease when  $\tau \in [0.0, 0.75]$  is mostly due to thermal-specific characteristics—e.g., the ghosting effect [9] which reduces sharpness and contrast in thermal images compared to RGB, making the pose reconstruction more difficult. For  $\tau \in [0.75, 1.0]$ , quality improves because the model increasingly operates in a near single-modality regime, reducing multimodal alignment complexity, while the larger number of thermal views provides stronger scene coverage for thermal reconstruction. The minimum occurs at  $\tau \approx 0.75$

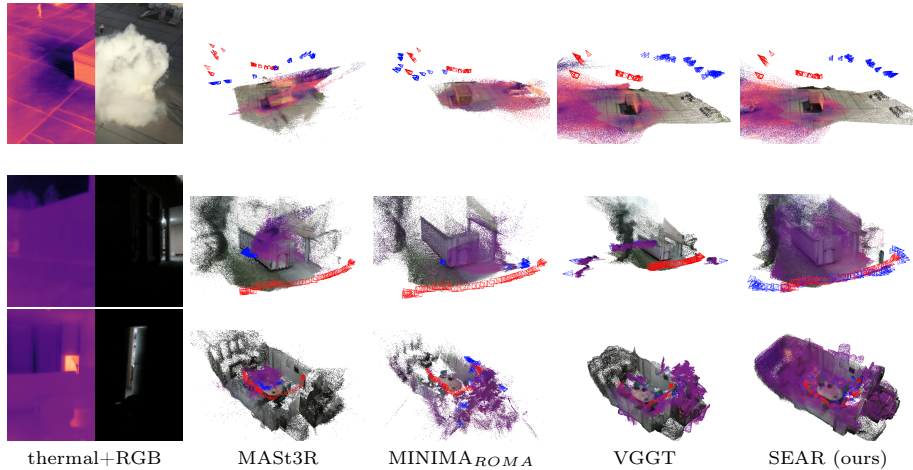


**Fig. 4:** Reconstructions from the SmokeSeer3D dataset (dense smoke, top) and our new dataset’s scenes (lighting changes, middle and bottom rows). The first column shows cases where RGB images (right) are unreliable for localization, so thermal images (left) are used. Our method recovers the scene even with smoke (SmokeSeer3D) and aligns RGB and thermal camera poses in different lighting conditions (our dataset).

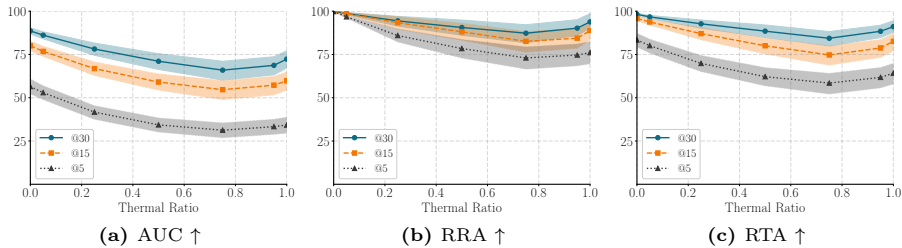


**Fig. 5:** The AUC, RRA, RTA (errors  $< 30^\circ$ ,  $15^\circ$ ,  $5^\circ$ ) across varying thermal-to-RGB image ratios. The filled area represents the boundary from 0.25– to 0.75–quantiles estimated by bootstrapping scenes 2000 times.

(rather than  $\tau = 0.5$ ) due to a trade-off: more thermal frames weaken pose cues, but a thermal-dominant input reduces cross-modal alignment and increases thermal view coverage. Depending on  $\tau$ , one effect can outweigh the other, which shifts the lowest point away from 0.5.

## 6.7 Thermal to RGB Alignment

In contrast to VGGT, we believe that our method explicitly keeps the distributions of thermal and RGB tokens in the AA module aligned. To validate this hypothesis, we feed RGB-thermal image pairs into our model and extract intermediate outputs from the AA module’s layers. We compute the cosine similarity [8] between same-level RGB and thermal tokens (excluding camera tokens). High similarity implies aligned distributions, while low similarity implies divergence. We compare RGB-

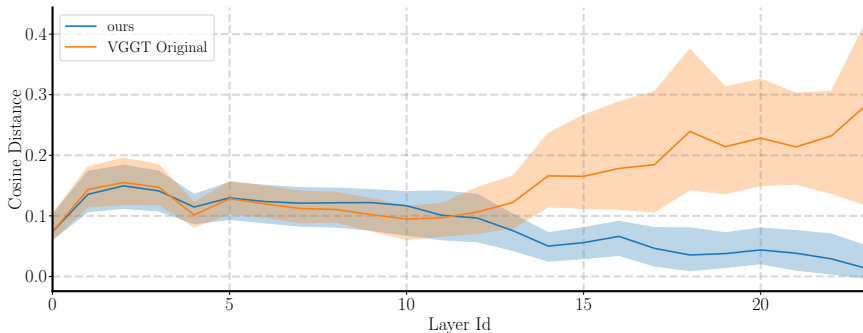


**Fig. 6:** The blue line represents the median difference between RGB-to-RGB and RGB-to-thermal cosine similarity dependence across layers for SEAR method. The orange line represents the same dependency for the VGGT model. The filled area represents the boundary from 0.25- to 0.75-quantiles.

to-RGB cosine similarity  $x_{r2r}$  (the baseline) to the cosine similarity  $x_{r2t}$  between RGB and thermal images. A large difference between  $x_{r2r}$  and  $x_{r2t}$  indicates a distribution mismatch, while a small difference suggests that the distributions are close. Experiments use a batch size of 12 and thermal ratios  $\tau \in [0.25, 0.75]$ .

Our results (Fig. 6) show that for the first 10 layers, both our model and VGGT show low RGB-thermal cosine similarity—interestingly, Bratulić et al. [1] demonstrated that VGGT reconstructs geometry post-layer10 of the AA-module. Beyond layer10, when the geometric reconstruction starts, VGGT’s difference between  $x_{r2r}$  and  $x_{r2t}$  increases, while ours remains consistently low, suggesting our model successfully aligned RGB and thermal token distributions for reconstruction in the whole AA module.

## 6.8 Ablation Studies

We perform extensive ablation studies to support our choice of architecture. We evaluate: 1) using the non-learnable rgb camera token instead of the learnable thermal camera token, 2) LLaVA [22]’s strategy (adding a learnable thermal projector of size 1024, initialized as the identity transformation, for thermal images), 3) adding a learnable thermal embedding, similar to positional embeddings in transformer [38] (initialized as zero to preserve the original model’s performance at the beginning of training), 4) only adding LoRA to global-attention layers, and 5) only applying LoRA to frame-attention layers.

We compute per-scene metrics over the public datasets and present their mean and standard deviation, as well as statistical analysis in Tab. 2 and Tab. 3. Our statistical analysis is a one-sided Welch’s t-test evaluating the null hypothesis that a given model (row) outperforms another (column) in terms of AUC@30. Our study reveals that incorporating a learnable thermal projector or learnable thermal embeddings does not improve performance. Specifically, our method has p-values of 0.05 (trend) and 0.02 (statistically significant) when compared to

**Table 2:** This figure shows the camera pose estimation metrics average and 95% confidence interval for the different ablation studies of our paper.

Method	AUC@30	RRA@30	RTA@30
No Camera Token	67.8 ± 1.4	89.1 ± 1.0	86.6 ± 1.3
Thermal Projector	67.2 ± 1.1	88.3 ± 0.8	86.0 ± 0.8
Thermal Modality Token	66.1 ± 1.8	87.6 ± 1.0	85.1 ± 1.2
Global Only	69.1 ± 1.5	89.4 ± 1.1	87.3 ± 1.6
Frame Only	62.4 ± 0.6	85.6 ± 0.9	83.0 ± 1.0
SEAR	68.4 ± 0.7	89.1 ± 0.5	86.9 ± 0.4

**Table 3: Pairwise statistical significance (AUC@30).** Each entry at position  $(i, j)$  reports the p-value from a one-sided Welch’s t-test for the null hypothesis that the row method outperforms the column method in AUC@30. Darker blue indicates smaller p-values (stronger evidence against the null).

	No Camera Token	Thermal Projector	Thermal Embedding	Global Only	Frame Only	Ours
No Camera Token	–	0.72	0.91	0.12	1.00	0.24
Thermal Projector	0.28	–	0.83	0.04	1.00	0.05
Thermal Embedding	0.09	0.17	–	0.02	1.00	0.02
Global Only	0.88	0.96	0.98	–	1.00	0.78
Frame Only	0.00	0.00	0.00	0.00	–	0.00
Ours	0.76	0.95	0.98	0.22	1.00	–

those models, supporting our decision to not include a learnable thermal projector or learnable thermal embeddings. For the no-camera-token model, the p-value of 0.24 does not invalidate the null hypothesis. However, when the no-camera-token model is evaluated against the thermal-embedding model, the p-value (0.09) only shows a trend, while our method achieves statistical significance ( $p = 0.02$ ). Similarly, the no-camera-token model shows no significant difference from the thermal-projector baseline ( $p = 0.28$ ), whereas our method reaches statistical significance ( $p = 0.05$ ). These results indicate that, although our architecture does not significantly outperform the no-camera-token model, it provides some improvements and greater stability when compared to other models.

Our method and the global-only model achieved comparable results in terms of statistical significance. While our analysis does not indicate a clear superiority of one approach over the other, future work could explore applying LoRA layers exclusively to the global attention layer—rather than both the global and frame layers—to further reduce parameter count without compromising performance.

## 7 Conclusion

In this work, we present SEAR, a simple and efficient framework to adapt visual geometric grounded transformers for RGB-T camera pose estimation and 3D scene reconstruction. By leveraging lightweight LoRA adapters, modality-specific camera tokens, and a carefully designed batching strategy, SEAR achieves state-of-the-art performance with minimal computational overhead and a modest amount of data, making it a practical solution for real-world applications. Our approach not only outperforms existing methods across all metrics but also demonstrates robustness in challenging real-world conditions such as low lighting, dense smoke, and asynchronous data capture. By showing that high-performance multimodal reconstruction is achievable with minimal adaptation and data, we hope to inspire broader adoption of parameter-efficient fine-tuning in geometric vision and beyond.

## Acknowledgements

We thank Ivan Skorokhodov for his assistance with writing, valuable feedback on earlier drafts of the paper, and help with several experiments. We also thank Martin Magnusson for valuable discussions and for suggesting several evaluation metrics and datasets.

## References

1. Bratulić, J., Mittal, S., Brox, T., Rupprecht, C.: On Geometric Understanding and Learned Data Priors in VGGT, (2025). arXiv: [2512.11508](https://arxiv.org/abs/2512.11508) [cs.CV]. <https://arxiv.org/abs/2512.11508> (cit. on p. 13).
2. Chassaing, E., Forest, F., Fink, O., Mielle, M.: Thermoxels: A Voxel-Based Method to Generate Simulation-Ready 3D Thermal Models. In: Journal of Physics: Conference Series. Journal of Physics: Conference Series (2025) (cit. on pp. 2, 3). <https://doi.org/10.48550/arXiv.2504.04448>. arXiv: [2504.04448](https://arxiv.org/abs/2504.04448). <http://arxiv.org/abs/2504.04448>
3. Edstedt, J., Sun, Q., Bökman, G., Wadenbäck, M., Felsberg, M.: Roma: Robust dense feature matching. In: Proceedings of the IEEE/CVF Conference on Computer Vision and Pattern Recognition, pp. 19790–19800 (2024) (cit. on pp. 9, 19, 27)
4. Elflein, S., Zhou, Q., Leal-Taixé, L.: Light3r-sfm: Towards feed-forward structure-from-motion. In: Proceedings of the IEEE/CVF Conference on Computer Vision and Pattern Recognition, pp. 16774–16784 (2025) (cit. on p. 9)
5. Fan, R., Zhao, W., Lin, M., Wang, Q., Liu, Y.-J., Wang, W.: Generalizable Thermal-based Depth Estimation via Pre-trained Visual Foundation Model. In: 2024 IEEE International Conference on Robotics and Automation (ICRA), pp. 14614–14621 (2024) (cit. on p. 5). <https://doi.org/10.1109/ICRA57147.2024.10610394>. <https://ieeexplore.ieee.org/document/10610394/>
6. Fischler, M.A., Bolles, R.C.: Random Sample Consensus: A Paradigm for Model Fitting with Applications to Image Analysis and Automated Cartography. Commun. ACM **24**(6), 381–395 (1981) (cit. on p. 3). <https://doi.org/10.1145/358669.358692>. <https://dl.acm.org/doi/10.1145/358669.358692>

7. Gretton, A., Borgwardt, K.M., Rasch, M.J., Schölkopf, B., Smola, A.: A Kernel Two-Sample Test. *Journal of Machine Learning Research* **13**(25), 723–773 (2012) (cit. on p. 30). <http://jmlr.org/papers/v13/gretton12a.html>
8. Han, J., Hong, S., Jung, J., Jang, W., An, H., Wang, Q., Kim, S., Feng, C.: Emergent Outlier View Rejection in Visual Geometry Grounded Transformers, (2025). arXiv: [2512.04012](https://arxiv.org/abs/2512.04012) [cs.CV]. <https://arxiv.org/abs/2512.04012> (cit. on p. 12).
9. Hassan, M., Forest, F., Fink, O., Mielle, M.: ThermoNeRF: A Multimodal Neural Radiance Field for Joint RGB-thermal Novel View Synthesis of Building Facades. *Advanced Engineering Informatics* **65**, 103345 (2025) (cit. on pp. 2, 3, 7, 11, 20–22). <https://doi.org/10.1016/j.aei.2025.103345>. <https://linkinghub.elsevier.com/retrieve/pii/S1474034625002381>
10. He, X., Yu, H., Peng, S., Tan, D., Shen, Z., Bao, H., Zhou, X.: Matchanything: Universal cross-modality image matching with large-scale pre-training. arXiv preprint arXiv:2501.07556 (2025) (cit. on pp. 9, 19)
11. Heusel, M., Ramsauer, H., Unterthiner, T., Nessler, B., Hochreiter, S.: GANs Trained by a Two Time-Scale Update Rule Converge to a Local Nash Equilibrium, (2018). arXiv: [1706.08500](https://arxiv.org/abs/1706.08500) [cs.LG]. <https://arxiv.org/abs/1706.08500> (cit. on p. 30).
12. Hounsby, N., Giurgiu, A., Jastrzebski, S., Morrone, B., De Laroussilhe, Q., Gesmundo, A., Attariyan, M., Gelly, S.: Parameter-Efficient Transfer Learning for NLP. In: *International Conference on Machine Learning*, pp. 2790–2799. PMLR (2019) (cit. on p. 3). <http://proceedings.mlr.press/v97/hounsby19a.html>
13. Hu, E.J., Shen, Y., Wallis, P., Allen-Zhu, Z., Li, Y., Wang, S., Wang, L., Chen, W., et al.: Lora: Low-rank adaptation of large language models. *ICLR* **1**(2), 3 (2022) (cit. on pp. 3, 5)
14. Hu, E.J., Shen, Y., Wallis, P., Allen-Zhu, Z., Li, Y., Wang, S., Wang, L., Chen, W.: LoRA: Low-Rank Adaptation of Large Language Models. In: *International Conference on Learning Representations* (2021) (cit. on p. 3). <https://openreview.net/forum?id=nZeVKeeFYf9>
15. Jain, N., Jong, A., Scherer, S., Gkioulekas, I.: SmokeSeer: 3D Gaussian Splatting for Smoke Removal and Scene Reconstruction. arXiv preprint arXiv:2509.17329 (2025) (cit. on pp. 8, 11)
16. Lee, A.J., Cho, Y., Shin, Y.-s., Kim, A., Myung, H.: ViViD++: Vision for visibility dataset. *IEEE Robotics and Automation Letters* **7**(3), 6282–6289 (2022) (cit. on p. 7)
17. Leroy, V., Cabon, Y., Revaud, J.: Grounding Image Matching in 3D with MAST3R. In: *Computer Vision – ECCV 2024*. Ed. by A. Leonardis, E. Ricci, S. Roth, O. Russakovsky, T. Sattler, and G. Varol, pp. 71–91. Springer Nature Switzerland, Cham (2025) (cit. on pp. 3, 8). [https://doi.org/10.1007/978-3-031-73220-1\\_5](https://doi.org/10.1007/978-3-031-73220-1_5). [https://link.springer.com/10.1007/978-3-031-73220-1\\_5](https://link.springer.com/10.1007/978-3-031-73220-1_5)
18. Lester, B., Al-Rfou, R., Constant, N.: The Power of Scale for Parameter-Efficient Prompt Tuning. In: Moens, M.-F., Huang, X., Specia, L., Yih, S.W.-t. (eds.) *Proceedings of the 2021 Conference on Empirical Methods in Natural Language Processing*, pp. 3045–3059. Association for Computational Linguistics, Online and Punta Cana, Dominican Republic (2021) (cit. on p. 3). <https://doi.org/10.18653/v1/2021.emnlp-main.243>. <https://aclanthology.org/2021.emnlp-main.243/>
19. Li, J., Li, Y., Sun, C., Wang, C., Xiang, J.: SPEC-NeRF: Multi-Spectral Neural Radiance Fields. In: *ICASSP 2024 - 2024 IEEE International Conference on Acoustics, Speech and Signal Processing (ICASSP)*, pp. 2485–2489 (2024) (cit.

- on p. 3). <https://doi.org/10.1109/ICASSP48485.2024.10446015>. <https://ieeexplore.ieee.org/document/10446015/>
20. Lin, Y.Y., Pan, X.-Y., Fridovich-Keil, S., Wetzstein, G.: Thermalnerf: Thermal radiance fields. In: 2024 IEEE International Conference on Computational Photography (ICCP), pp. 1–12 (2024) (cit. on pp. 2, 3, 7, 22, 24)
  21. Lin, Y.Y., Pan, X.-Y., Fridovich-Keil, S., Wetzstein, G.: ThermalNeRF: Thermal Radiance Fields, (2024). arXiv: 2407.15337 [cs.CV]. <https://arxiv.org/abs/2407.15337> (cit. on pp. 2, 7).
  22. Liu, H., Li, C., Wu, Q., Lee, Y.J.: Visual instruction tuning. *Advances in neural information processing systems* **36**, 34892–34916 (2023) (cit. on p. 13)
  23. Liu, Y., Chen, X., Yan, S., Cui, Z., Xiao, H., Liu, Y., Zhang, M.: ThermalGS: Dynamic 3D Thermal Reconstruction with Gaussian Splatting. *Remote Sensing* **17**(2), 335 (2025) (cit. on p. 3). <https://doi.org/10.3390/rs17020335>. <https://www.mdpi.com/2072-4292/17/2/335>
  24. Mi, L., Wang, W., Tu, W., He, Q., Kong, R., Fang, X., Dong, Y., Zhang, Y., Li, Y., Li, M., Dai, H., Chen, G., Liu, Y.: Empower Vision Applications with LoRA LMM. In: Proceedings of the Twentieth European Conference on Computer Systems. EuroSys '25, pp. 261–277. Association for Computing Machinery, New York, NY, USA (2025) (cit. on p. 3). <https://doi.org/10.1145/3689031.3717472>. <https://dl.acm.org/doi/10.1145/3689031.3717472>
  25. Morelli, L., Ioli, F., Maiwald, F., Mazzacca, G., Menna, F., Remondino, F.: DEEP-IMAGE-MATCHING: A TOOLBOX FOR MULTIVIEW IMAGE MATCHING OF COMPLEX SCENARIOS. *The International Archives of the Photogrammetry, Remote Sensing and Spatial Information Sciences* **XLVIII-2/W4-2024**, 309–316 (2024) (cit. on p. 9). <https://doi.org/10.5194/isprs-archives-XLVIII-2-W4-2024-309-2024>
  26. Mur-Artal, R., Montiel, J.M.M., Tardós, J.D.: ORB-SLAM: A Versatile and Accurate Monocular SLAM System. *IEEE Transactions on Robotics* **31**(5), 1147–1163 (2015) (cit. on p. 3). <https://doi.org/10.1109/TR0.2015.2463671>. <https://ieeexplore.ieee.org/abstract/document/7219438>
  27. Oquab, M., Darcet, T., Moutakanni, T., Vo, H., Szafraniec, M., Khalidov, V., Fernandez, P., Haziza, D., Massa, F., El-Nouby, A., et al.: Dinov2: Learning robust visual features without supervision. arXiv preprint arXiv:2304.07193 (2023) (cit. on pp. 3, 5)
  28. Özer, M., Weiherer, M., Hundhausen, M., Egger, B.: Exploring multi-modal neural scene representations with applications on thermal imaging. In: European Conference on Computer Vision, pp. 82–98 (2024) (cit. on pp. 7, 22, 23)
  29. Ren, J., Jiang, X., Li, Z., Liang, D., Zhou, X., Bai, X.: MINIMA: Modality Invariant Image Matching. arXiv preprint arXiv:2412.19412 (2024) (cit. on pp. 9, 19)
  30. Sarlin, P.-E., DeTone, D., Malisiewicz, T., Rabinovich, A.: SuperGlue: Learning feature matching with graph neural networks. In: Proceedings of the IEEE/CVF conference on computer vision and pattern recognition, pp. 4938–4947 (2020) (cit. on p. 8)
  31. Schonberger, J.L., Frahm, J.-M.: Structure-from-Motion Revisited. In: Proceedings of the IEEE Conference on Computer Vision and Pattern Recognition, pp. 4104–4113 (2016) (cit. on pp. 2, 3, 8). [https://www.cv-foundation.org/openaccess/content\\_cvpr\\_2016/html/Schonberger\\_Structure-From-Motion\\_Revisited\\_CVPR\\_2016\\_paper.html](https://www.cv-foundation.org/openaccess/content_cvpr_2016/html/Schonberger_Structure-From-Motion_Revisited_CVPR_2016_paper.html)

32. Shin, U., Park, J., Kweon, I.S.: Deep Depth Estimation From Thermal Image. In: Proceedings of the IEEE/CVF Conference on Computer Vision and Pattern Recognition, pp. 1043–1053 (2023) (cit. on p. 7)
33. Skorokhodov, V., Mielle, M., (2026). <https://doi.org/10.5281/zenodo.19057885> (cit. on p. 6).
34. Sun, S., Mielle, M., Lilienthal, A.J., Magnusson, M.: High-Fidelity SLAM Using Gaussian Splatting with Rendering-Guided Densification and Regularized Optimization. In: 2024 IEEE International Conference on Intelligent Robots and Systems (IROS). IEEE, Abu Dhabi, UAE (2024) (cit. on p. 3). arXiv: [2403.12535](https://arxiv.org/abs/2403.12535). <http://arxiv.org/abs/2403.12535>
35. Teledyne FLIR, FLIR One<sup>®</sup> Pro Thermal Imaging Camera for Smartphones, Accessed: 2026-02-05. Teledyne FLIR LLC. (2026). <https://www.flir.com/products/flir-one-pro/> (cit. on pp. 6, 20)
36. Tuzcuoglu, Ö., Köksal, A., Sofu, B., Kalkan, S., Alatan, A.A.: Xoftr: Cross-modal feature matching transformer. In: Proceedings of the IEEE/CVF conference on computer vision and pattern recognition, pp. 4275–4286 (2024) (cit. on pp. 2, 26)
37. Umeyama, S.: Least-squares estimation of transformation parameters between two point patterns. IEEE Transactions on Pattern Analysis and Machine Intelligence **13**(4), 376–380 (1991) (cit. on p. 9). <https://doi.org/10.1109/34.88573>
38. Vaswani, A., Shazeer, N., Parmar, N., Uszkoreit, J., Jones, L., Gomez, A.N., Kaiser, Ł., Polosukhin, I.: Attention is all you need. Advances in neural information processing systems **30** (2017) (cit. on p. 13)
39. Wang, J., Chen, M., Karaev, N., Vedaldi, A., Rupprecht, C., Novotny, D.: Vggt: Visual geometry grounded transformer. In: Proceedings of the Computer Vision and Pattern Recognition Conference, pp. 5294–5306 (2025) (cit. on pp. 2–4, 9)
40. Wang, S., Leroy, V., Cabon, Y., Chidlovskii, B., Revaud, J.: Dust3r: Geometric 3d Vision Made Easy. In: Proceedings of the IEEE/CVF Conference on Computer Vision and Pattern Recognition, pp. 20697–20709 (2024) (cit. on pp. 3, 8). [http://openaccess.thecvf.com/content/CVPR2024/html/Wang\\_DUST3R\\_Geometric\\_3D\\_Vision\\_Made\\_Easy\\_CVPR\\_2024\\_paper.html](http://openaccess.thecvf.com/content/CVPR2024/html/Wang_DUST3R_Geometric_3D_Vision_Made_Easy_CVPR_2024_paper.html)
41. Wang, Y., He, X., Peng, S., Tan, D., Zhou, X.: Efficient LoFTR: Semi-Dense Local Feature Matching with Sparse-Like Speed, (2024). arXiv: [2403.04765](https://arxiv.org/abs/2403.04765) [cs.CV]. <https://arxiv.org/abs/2403.04765> (cit. on pp. 9, 19).
42. Waseem, A., Mielle, M.: Physics-Informed Neural Networks for Thermophysical Property Retrieval, (2025). arXiv: [2511.23449](https://arxiv.org/abs/2511.23449) [cs]. <http://arxiv.org/abs/2511.23449>. Pre-published (cit. on p. 2). <https://doi.org/10.48550/arXiv.2511.23449>
43. Wu, Y., Hu, Z.: PnP Problem Revisited. Journal of Mathematical Imaging and Vision **24**(1), 131–141 (2006) (cit. on p. 3). [https://idp.springer.com/authorize/casa?redirect\\_uri=https://link.springer.com/article/10.1007/s10851-005-3617-z&casa\\_token=mCtcAUemRv4AAAAA:jX9kDIPKfHxykhn7-1fR\\_nup04X0\\_4cM5EUI16wot8SHlckWcE4qhgYw7gIRnv7IjiT0yKYqa754hlUZw](https://idp.springer.com/authorize/casa?redirect_uri=https://link.springer.com/article/10.1007/s10851-005-3617-z&casa_token=mCtcAUemRv4AAAAA:jX9kDIPKfHxykhn7-1fR_nup04X0_4cM5EUI16wot8SHlckWcE4qhgYw7gIRnv7IjiT0yKYqa754hlUZw)
44. Xu, J., Liao, M., Kathirvel, R.P., Patel, V.M.: Leveraging Thermal Modality to Enhance Reconstruction in Low-Light Conditions. In: Leonardis, A., Ricci, E., Roth, S., Russakovsky, O., Sattler, T., Varol, G. (eds.) Computer Vision – ECCV 2024, pp. 321–339. Springer Nature Switzerland, Cham (2025) (cit. on p. 2). [https://doi.org/10.1007/978-3-031-72913-3\\_18](https://doi.org/10.1007/978-3-031-72913-3_18)
45. Yuan, J., Li, H., Ding, X., Xie, W., Li, Y.-J., Zhao, W., Wan, K., Shi, J., Hu, X., Liu, Z.: Understanding and Mitigating Numerical Sources of Nondeterminism in LLM Inference, (2025). arXiv: [2506.09501](https://arxiv.org/abs/2506.09501) [cs]. <http://arxiv.org/abs/2506.09501>. Pre-published (cit. on p. 8). <https://doi.org/10.48550/arXiv.2506.09501>

## Appendix

### A Implementation Details

We use the COLMAP + SuperPoint + SuperGlue pipeline provided in `nerfstudio`, with the default hyperparameters.

For DUST3R and MAST3R, we use the official implementations from their respective GitHub repositories. These models first estimate relative camera poses and depths for pairs of input images, and then perform global optimization to recover the final camera poses and depths. The authors provide flexible control over the image pairing strategy. To avoid CUDA out-of-memory issues, we use the `noncyclic-logwin` scene graph with a window size of 5. Specifically, for each image at index  $i$ , this strategy creates image pairs  $(i - 2^5, i), (i - 2^4, i), \dots, (i + 2^4, i), (i + 2^5, i)$  instead of constructing a complete graph over all possible image pairs. This design preserves substantial overlap between paired views while significantly reducing computational and memory requirements.

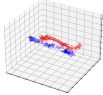
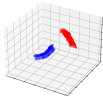
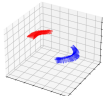
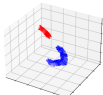
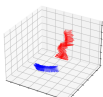
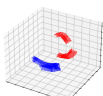
MINIMA [29] provides several multimodal image matching models trained with the authors’ proposed strategy. Among them, we select the official ROMA [3]-based checkpoint, denoted as `MINIMAROMA`, since it achieves the best performance. Match-Anything [10] reports results for multiple models trained using its proposed framework. However, among the officially released checkpoints, only the Efficient-LoFTR [41]-based model, denoted as `MAELoFTR`, is publicly available. We therefore use this model as a baseline. For a fair comparison and to reduce computational cost, we adopt the same image pairing strategy for `MAELoFTR` and `MINIMAROMA` as used for MAST3R and DUST3R.

### B SEAR Dataset

**Table 4:** Detailed description of the datasets and split used for training and for evaluation.

Dataset	#Training Scenes	#Evaluation Scenes	Aligned modalities	Cross positional	Cross temporal	Ground Truth
For training and quantitative evaluation						
ThermoScenes	15	5	True	True	False	VGGT
ThermalGaussians	11	3	True	True	False	VGGT
ThermalMix	4	2	True	True	False	VGGT
ThermalNeRF	8	2	False	True	False	VGGT
RF	9	6	True	True	False	Motion Capture
<b>Total</b>	<b>47</b>	<b>18</b>				
For qualitative evaluation only						
SmokeSeer3D	0	2	False	True	True	None
Ours (same light)	0	6	True	True	True	VGGT
Ours (different lighting conditions)	0	3	True	False	True	None
<b>Total</b>	<b>0</b>	<b>11</b>				

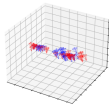
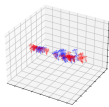
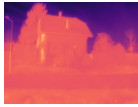
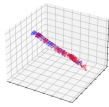
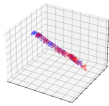
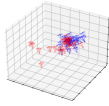
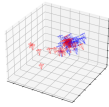
**Table 5:** Summary of the SEAR dataset for well-lit scenes, where both trajectories are captured under the same bright illumination conditions. The figure includes RGB and thermal images, two camera trajectories obtained by running VGGT on the RGB images, the lengths of the two trajectories, and the minimum and maximum temperatures.

Scene	RGB	Thermal	Trajectory	Length 1 Length 2	Temp. min Temp. max
conference-room				34 35	12.9°C 30.8°C
metallic-container				50 80	-6.8°C 5.6°C
parking				40 43	-6.8°C 13.1°C
statue				70 37	-9.6°C 4.9°C
telescope				42 54	-46.3°C* 13.4°C
old-drinking-fountain				70 54	-8.0°C 12.5°C

We collect a dataset comprising nine scenes using the FLIR One Pro LT camera [35]. A comparison with other datasets is provided in Tab. 4. The camera operates within  $[-20^{\circ}\text{C}, 120^{\circ}\text{C}]$  with a thermal accuracy of  $\pm 3^{\circ}\text{C}$ . We estimate the thermal precision following the procedure described in ThermoNeRF [9], and find that this characteristic matches the  $\pm 0.14^{\circ}\text{C}$  reported in ThermoNeRF. We follow the postprocessing instructions from ThermoNeRF to extract RGB and thermal values from raw images.

Each scene capture consists of two trajectories. For six scenes (**conference-room**, **metallic-container**, **parking**, **statue**, **telescope**, **old-drinking-fountain**), the trajectories do not intersect and are recorded under the same favorable lighting conditions (see summary in Tab. 5). For the remaining three scenes (**red-container**, **house**, **messy-living-room**), the trajectories intersect and are captured under different lighting conditions—one trajectory is well lit, while the other is poorly lit (see summary in Tab. 6). In the latter case, the RGB images

**Table 6:** Summary of the SEAR dataset dataset for poorly lit scenes, where the trajectories are captured under different lighting conditions. The figure includes RGB and thermal images, the camera trajectory estimated by running VGGT on the thermal images (and is therefore less accurate), the lengths of the two trajectories, and the minimum and maximum temperatures for each trajectory.

Scene	Well-Lit	RGB	Thermal	Trajectory	Length	Temp. min Temp. max
red-container	True				55	-7.0°C 6.8°C
	False				60	-8.6°C 6.4°C
house	True				60	-38.4°C* 13.6°C
	False				60	-45.0°C* 33.4°C
messy-living-room	True				52	10.5°C 36.4°C
	False				49	10.2°C 38.8°C

from the poorly lit trajectory are dark and therefore unsuitable for localization. For `telescope` and `house` scenes, the minimal temperature is lower than the camera’s minimum operating bound of  $-20^{\circ}\text{C}$  due to the radiation in atmospheric radiation in the sky (the same effect as in [9])

## C Using COLMAP to Estimate Ground Truth Camera Poses

While our work prioritizes improving VGGT’s multimodal reconstruction performance rather than its general pose estimation capabilities, we provide camera estimation metrics. As stated in the paper, we benchmark against VGGT-derived poses—except for RF Dataset, where motion-capture produces camera poses. For each scene of  $N$  image pairs, we use  $N$  RGB only images for ground truth pose

**Table 7:** Qualitative comparison of 3D reconstruction on **ThermoScenes** [9] if COLMAP is used to estimate ground truth camera poses.

Method	prpt-cup					INR-building				
	AUC ↑	RRA ↑	RTA ↑	Reg (%) ↑	FPS ↑	AUC ↑	RRA ↑	RTA ↑	Reg (%) ↑	FPS ↑
COLMAP + SPSG	49.4	73.7	75.3	51.2	0.40	34.9	52.3	57.6	49.7	0.49
MA <sub>ELOFTR</sub>	16.3	70.0	45.0	4.0	0.18	2.6	61.6	13.6	15.6	0.19
MINIMA <sub>ROMA</sub>	8.4	26.6	31.3	100.0	0.02	15.3	48.2	42.0	100.0	0.03
DUST3R	19.9	29.2	32.9	100.0	0.43	6.5	44.6	33.9	100.0	0.66
MASt3R	22.5	54.9	44.3	100.0	0.14	3.7	24.4	24.7	100.0	0.25
VGGT	15.9	59.0	37.2	100.0	4.09	9.4	47.7	34.5	100.0	4.91
SEAR	82.4	100.0	97.8	100.0	2.65	20.4	48.2	48.6	100.0	4.79

Method	reflect-robot					melting_ice_cup				
	AUC ↑	RRA ↑	RTA ↑	Reg (%) ↑	FPS ↑	AUC ↑	RRA ↑	RTA ↑	Reg (%) ↑	FPS ↑
COLMAP + SPSG	6.2	66.3	28.4	29.0	0.54	0.7	13.1	21.6	25.8	0.56
MA <sub>ELOFTR</sub>	16.8	79.7	44.8	11.3	0.16	4.1	26.6	22.3	8.8	0.28
MINIMA <sub>ROMA</sub>	60.2	89.8	85.6	100.0	0.04	6.2	16.9	21.7	100.0	0.03
DUST3R	13.4	37.1	29.2	100.0	0.66	17.1	39.6	40.7	100.0	0.68
MASt3R	23.9	79.9	33.2	100.0	0.24	25.3	36.2	49.0	100.0	0.24
VGGT	16.6	45.3	38.4	100.0	4.94	19.4	38.4	42.0	100.0	6.81
SEAR	64.5	93.9	93.2	100.0	4.81	35.5	49.0	64.2	100.0	6.59

Method	freezing_ice_cup				
	AUC ↑	RRA ↑	RTA ↑	Reg (%) ↑	FPS ↑
COLMAP + SPSG	38.6	57.1	63.4	50.0	0.52
MA <sub>ELOFTR</sub>	4.3	30.6	40.5	7.6	0.33
MINIMA <sub>ROMA</sub>	6.1	12.1	26.5	100.0	0.04
DUST3R	15.0	29.9	42.4	100.0	0.66
MASt3R	18.6	38.6	40.8	100.0	0.22
VGGT	10.8	26.6	34.2	100.0	4.89
SEAR	18.3	33.5	45.8	100.0	4.76

estimation, and  $\frac{1}{2}N$  RGB and  $\frac{1}{2}N$  thermal images in the test phase. This approach guarantees both ground truth accuracy and sufficient differences between the test and ground truth sets.

We selected VGGT over alternatives like COLMAP for two key reasons: 1) VGGT authors’ reported higher accuracy of their model on camera pose estimation, and 2) empirical limitations of COLMAP. For example, COLMAP estimated poses for the **INR-building** scene (ThermoScenes) are misaligned (visual inspection showed that many cameras are incorrectly oriented). However, to avoid possible bias due to the use of VGGT for ground truth estimation, we include here comparative results using COLMAP-derived ground truth where available (i.e., for ThermoScenes [9], ThermalMix [28], and ThermalGaussian [20])—per-scene results are provided in Tab. 7, Tab. 9, and Tab. 8.

Results on COLMAP-estimated camera poses are similar to those obtained using VGGT-estimated poses in the main paper: according to the quantitative metrics, SEAR achieves improved multimodal geometry reconstruction compared

**Table 8:** Qualitative comparison of 3D reconstruction on **ThermalMix** [28] if COLMAP is used to estimate ground truth camera poses.

Method	laptop					panel				
	AUC $\uparrow$	RRA $\uparrow$	RTA $\uparrow$	Reg (%) $\uparrow$	FPS $\uparrow$	AUC $\uparrow$	RRA $\uparrow$	RTA $\uparrow$	Reg (%) $\uparrow$	FPS $\uparrow$
COLMAP + SPSG	56.6	100.0	90.9	10.8	0.28	17.6	32.2	48.3	28.0	0.32
MA <sub>ELOFTR</sub>	23.2	51.1	61.5	48.9	0.15	46.0	73.6	98.1	35.4	0.36
MINIMA <sub>ROMA</sub>	78.5	94.8	94.3	100.0	0.04	78.4	95.2	93.2	100.0	0.05
DUST3R	21.1	44.1	46.1	100.0	0.67	15.5	70.4	39.4	100.0	0.65
MASt3R	30.0	62.5	74.8	100.0	0.23	35.7	67.1	68.2	100.0	0.23
VGGT	15.3	30.8	41.3	100.0	11.23	12.7	28.5	45.2	100.0	17.04
SEAR	90.5	100.0	99.5	100.0	10.70	82.2	100.0	99.3	100.0	15.72

with the baselines. Our conclusions are consistent across different ground truth poses.

## D Additional Visual Comparisons

In this section, we provide additional visual comparisons with the baselines. For each evaluation scene, we randomly select either its first or second validation run. We present the results for SEAR dataset in Fig. 7, RF in Fig. 8, ThermalGaussian in Fig. 9, ThermalMix in Fig. 10, ThermalNeRF in Fig. 11, and ThermoScenes in Fig. 12. COLMAP tends to reconstruct only one modality. MA<sub>ELOFTR</sub> provides an insufficient number of matches for reliable reconstruction, while MINIMA<sub>ROMA</sub> often produces noisy reconstructions. DUST3R, MASt3R, and VGGT tend to reconstruct the two modalities as separate, unaligned point clouds. In contrast, the reconstructions produced by SEAR are cleaner, more accurate, and contain fewer artifacts, with camera poses that are also closer to the ground truth.

We also provide additional qualitative results for the best-performing methods on the qualitative-only datasets SmokeSeer in Fig. 14 and SEAR dataset (with trajectories captured at different times) in Fig. 13. The behavior of our method and the baselines is consistent with the observations discussed in the previous paragraph. On SmokeSeer, all methods fail to reconstruct **red-container**. A possible reason is that the thermal images contain overlaid printed statistics, which may negatively affect the models since the text regions can be erroneously interpreted as localization features.

## E Per-Scene Comparison

In this section, we present per-scene results of our method and the baselines. We present the results separately for SEAR dataset in Tab. 10, RF in Tab. 11, ThermalGaussian in Tab. 12, ThermalMix in Tab. 15, ThermalNeRF in Tab. 13, and ThermoScenes in Tab. 14.

**Table 9:** Qualitative comparison of 3D reconstruction on **ThermalGaussian** [20] if COLMAP on RGB is ground truth.

Method	IronIngot					Parterre				
	AUC $\uparrow$	RRA $\uparrow$	RTA $\uparrow$	Reg (%) $\uparrow$	FPS $\uparrow$	AUC $\uparrow$	RRA $\uparrow$	RTA $\uparrow$	Reg (%) $\uparrow$	FPS $\uparrow$
COLMAP + SPSG	96.0	100.0	99.7	100.0	0.54	46.0	100.0	100.0	3.0	0.53
MA <sub>ELOFTR</sub>	13.7	56.0	58.5	61.5	0.12	32.0	66.8	85.5	24.2	0.23
MINIMA <sub>ROMA</sub>	97.4	100.0	99.9	100.0	0.06	34.4	47.5	64.1	100.0	0.04
DUST3R	15.5	75.0	39.6	100.0	0.66	43.1	95.3	79.5	100.0	0.65
MASt3R	74.2	100.0	96.7	100.0	0.23	86.0	100.0	98.8	100.0	0.22
VGGT	31.8	68.5	69.8	100.0	14.13	65.5	87.2	85.9	100.0	13.81
SEAR	87.2	100.0	98.1	100.0	13.34	94.6	100.0	100.0	100.0	13.01

Method	Ebike				
	AUC $\uparrow$	RRA $\uparrow$	RTA $\uparrow$	Reg (%) $\uparrow$	FPS $\uparrow$
COLMAP + SPSG	65.0	70.2	70.4	95.8	0.60
MA <sub>ELOFTR</sub>	44.6	77.8	66.7	7.3	0.38
MINIMA <sub>ROMA</sub>	94.3	100.0	100.0	100.0	0.07
DUST3R	20.0	29.7	35.9	100.0	0.65
MASt3R	90.3	100.0	99.5	100.0	0.24
VGGT	83.9	100.0	98.0	100.0	16.06
SEAR	95.2	100.0	100.0	100.0	15.07

The per-scene results confirm the conclusions of the main evaluation. SEAR is the only method that consistently achieves both high pose accuracy and point cloud quality across a wide range of scenes, which translates into reliable multimodal reconstruction. Although COLMAP obtains strong scores on some scenes, these results are often artificially inflated, since COLMAP frequently reconstructs only one modality and registers only a subset of the frames. Likewise, MA<sub>ELOFTR</sub> usually provides too few matches for robust estimation, resulting in low registration rates and weak 3D reconstruction.

Among the remaining baselines, MINIMA<sub>ROMA</sub> is the strongest competitor, but it still produces noisier and less stable reconstructions than SEAR. DUST3R, MASt3R, and VGGT are not designed for RGB-T reconstruction and tend to recover separate, unaligned point clouds for the two modalities instead of a single coherent scene geometry, which negatively influences the reconstruction scores. By contrast, SEAR reconstructs cleaner geometry and estimates camera poses that are closer to the ground truth, leading to the most consistent overall performance in the per-scene comparison.

## F Two-View Camera Pose Estimation

Because we vary the sequence length during training, our method naturally extends to the two-view setting for estimating the relative pose between a pair

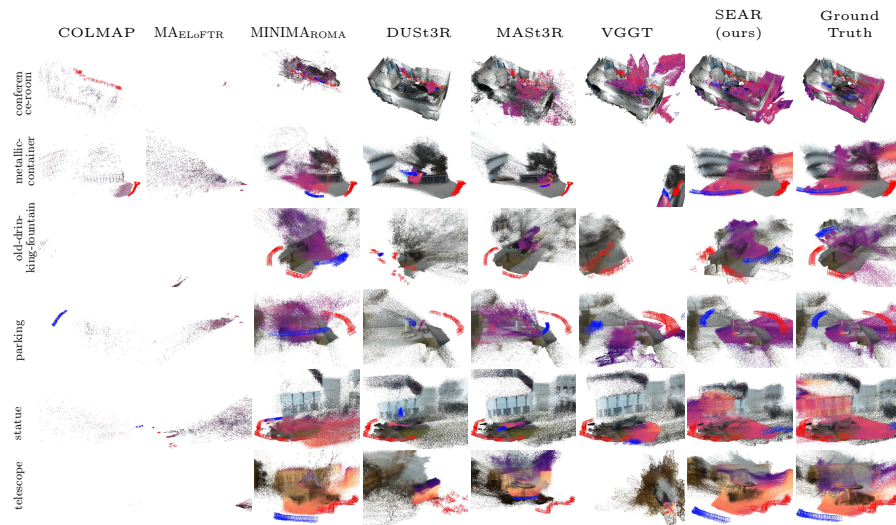


**Fig. 7:** Qualitative results on SEAR dataset. Our method produces more accurate and structurally consistent point clouds than the baselines. All methods show limited performance on `conference-room` and `old-drinking-fountain`, likely because the thermal modality in these scenes provides weak localization cues.

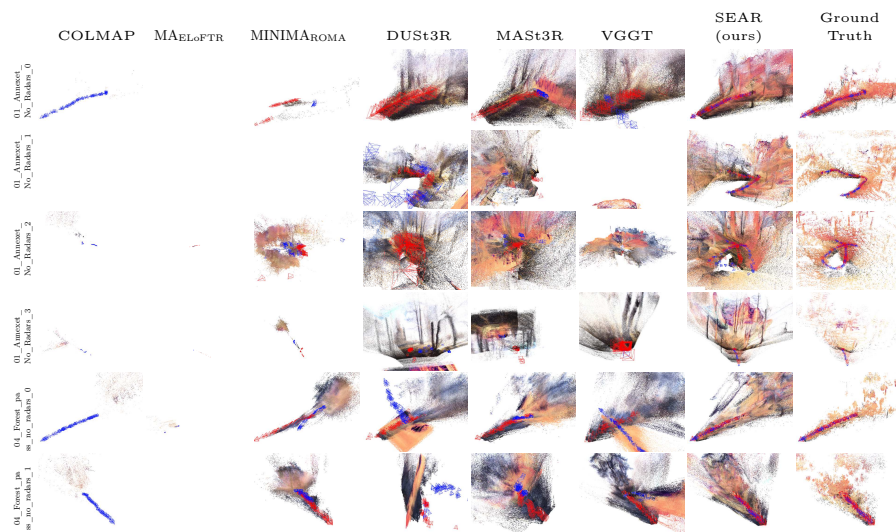


**Fig. 8:** Qualitative results on the RF dataset. Our method produces more accurate point clouds than the baselines. All methods show degraded performance on `01_Annexet_No_Radars_1` and `01_Annexet_No_Radars_2`, likely due to the complex camera motion in these sequences.

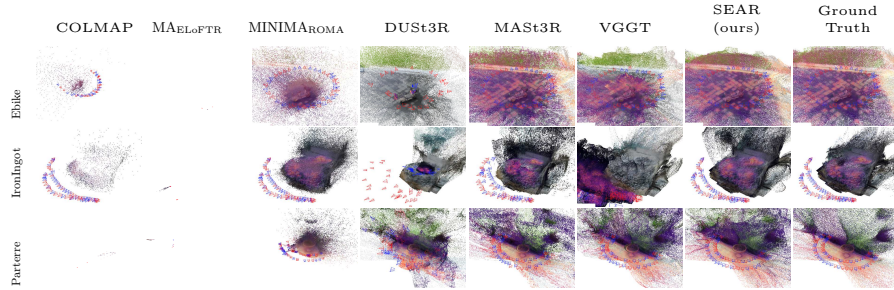


**Fig. 9:** Qualitative results on the ThermalGaussian dataset. Our method produces more accurate point clouds than the baselines on *Ebike* and *Parterre*. For *Iron Ingot*, our reconstruction is visually highly accurate, although its quantitative metrics are lower than those of COLMAP and MINIMAROMA.

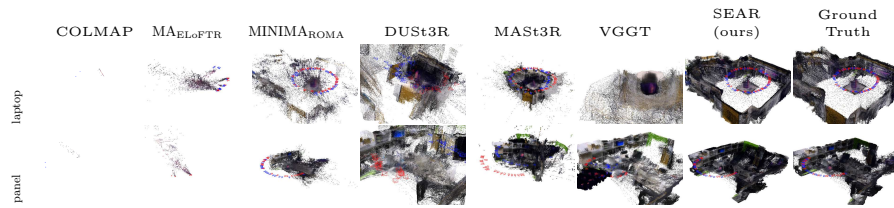


**Fig. 10:** Qualitative results on the ThermalMix dataset. Our method produces more accurate and complete point clouds than the baselines.

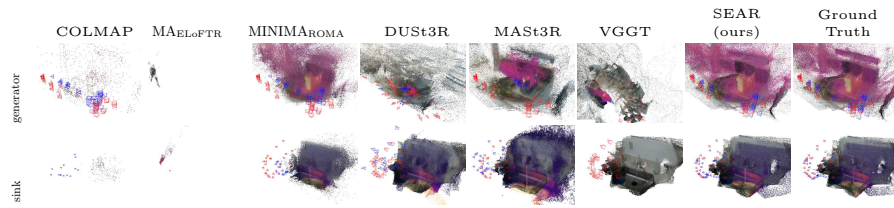


**Fig. 11:** Qualitative results on the ThermalNeRF dataset. Our method produces more accurate and structurally coherent point clouds than the baselines.

of multimodal images. Unlike multimodal camera pose estimation on image sets (presented in the *Multimodal Camera Pose Estimation* subsection of the main paper), evaluating MINIMAROMA and MAELoFTR in the two-view setting does not require **deep-image-matching**, since the relative pose can be recovered directly from 2D–2D correspondences via the essential matrix. This evaluation is important because it allows us to compare SEAR and matching-based methods without relying on the **deep-image-matching** framework.

We use the widely adopted MeTU-VisTIR dataset [36] to benchmark the methods. In contrast, the collected SEAR dataset and Public datasets are not easily adaptable to two-view evaluation, because it is difficult to sample representative image pairs for a fair comparison.

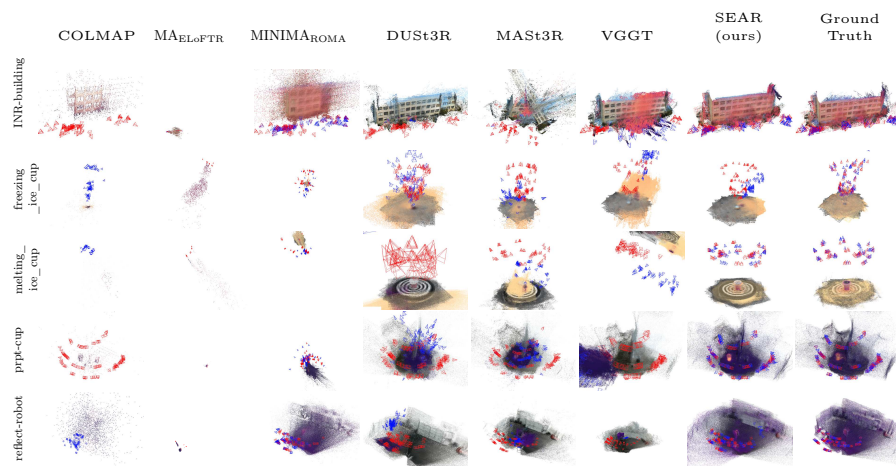


**Fig. 12:** Qualitative results on the ThermoScenes dataset. Our method produces more accurate point clouds than the baselines. All methods demonstrate limited performance on `freezing_ice_cup`, likely because of the inherent difficulty of this scene, discussed in Sec. C.

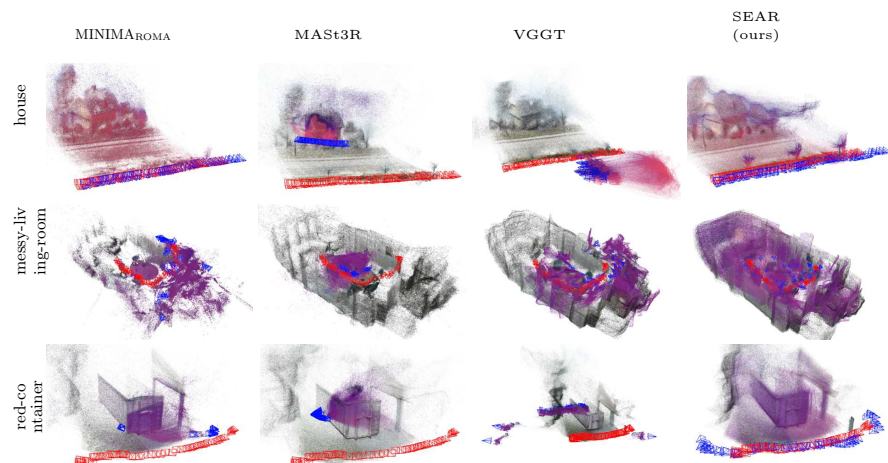


**Fig. 13:** Qualitative results on SEAR dataset, where the trajectories were captured under different lighting conditions. Our method produces more accurate point clouds than the baselines. Although `MINIMA_ROMA` achieves competitive performance on `house`, it fails on the remaining scenes.

To evaluate `MINIMA_ROMA` and `MA_ELoFTR`, we first extract correspondences between a multimodal image pair, then estimate the essential matrix using the known camera intrinsics, following RoMA [3], and finally recover the relative camera pose. For SEAR, we feed the image pair directly into the model and

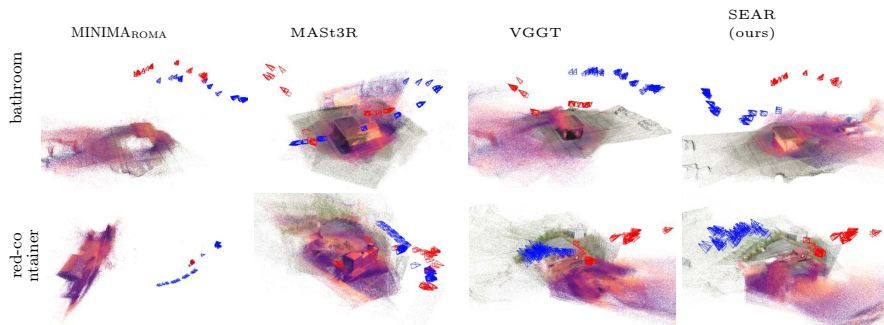


**Fig. 14:** Qualitative results on the SmokeSeer dataset. Our method produces more accurate point clouds than the baselines. All methods do not reconstruct **red-container**, likely because the overlaid text in the thermal images introduces misleading localization cues.

estimate the relative pose without using known intrinsics, relying solely on the model predictions.

The results are presented in Tab. 16. SEAR outperforms all competing methods by a large margin on nearly all metrics, with the exception of RRA@20, where it achieves a result slightly higher than MINIMAROMA. VGGT is not designed for multimodal camera pose estimation and therefore performs poorly, while MA<sub>ELoFTR</sub> finds too few matches to enable accurate estimation. These results show that SEAR is not only effective for RGB-thermal geometry reconstruction on image sets, but also highly competitive for two-view relative camera pose estimation.

## G Thermal to RGB alignment

In this section, we present additional results demonstrating the alignment between RGB and thermal features in our model.

Our analysis suggests that the model does not learn a completely new representation for mixed-modality inputs, but instead operates largely within the original VGGT feature space. To support this claim, we run SEAR on RGB-thermal inputs and the original VGGT on the corresponding RGB-only images, and extract the intermediate outputs of the frame-attention layers in the AA modules. We then perform Principal Component Analysis (PCA) on features from the same layer and visualize the resulting embeddings in Fig. 15. It can be observed that, at each layer, the RGB features produced by SEAR and the original pre-trained VGGT model exhibit very similar structures. The **layers 12-14** clearly show how our model aligns RGB and thermal features. After **layer14**, the combined RGB and thermal features closely resembles the RGB features produced by the pre-trained VGGT model for RGB-only images.

We also measure the discrepancy between the distributions of thermal and RGB tokens using the KL divergence (specifically its symmetrized form, also

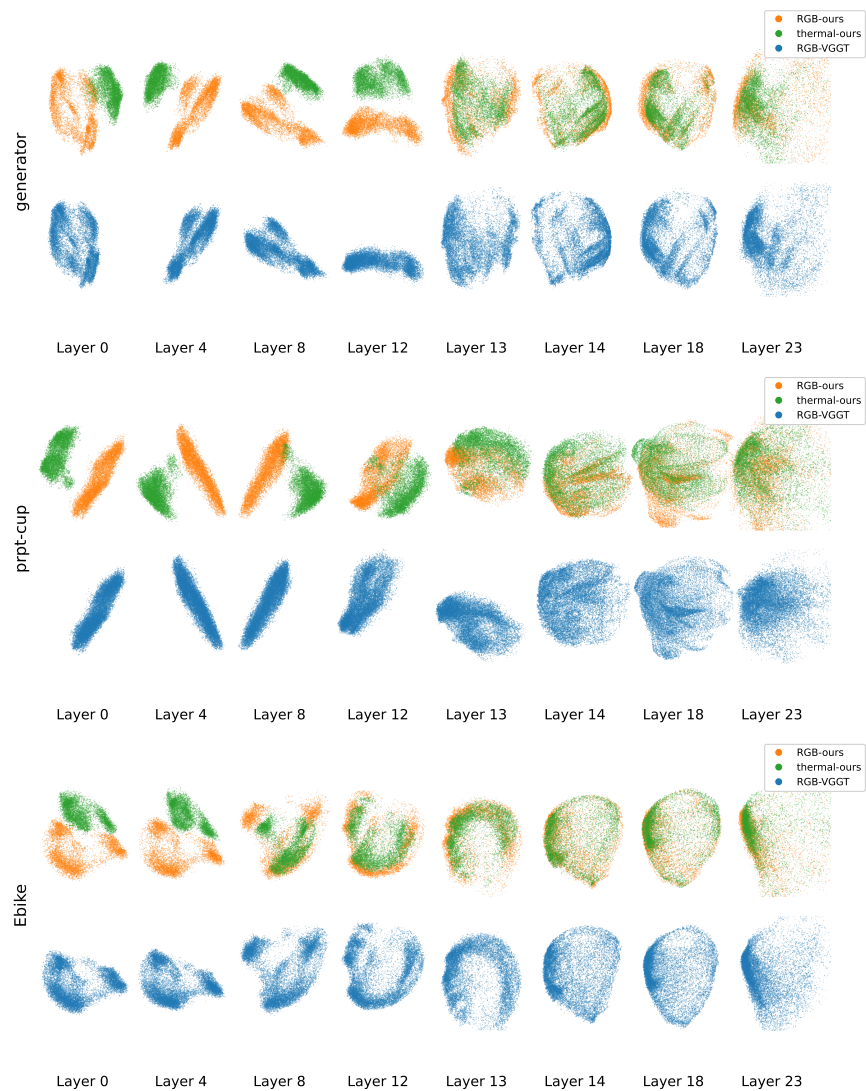


**Fig. 15:** PCA-based analysis of RGB-thermal feature alignment. The figure shows three experiments: **generator** from ThermalNeRF (rows 1-2), **prpt-cup** from ThermoScenes (rows 3-4), and **Ebike** from ThermalGaussian (rows 5-6). For each experiment, the top row illustrates the feature evolution of our model on RGB-thermal inputs, while the bottom row shows the feature evolution of VGGT on the corresponding RGB-only inputs.

**Table 10:** Per-scene metrics on SEAR dataset. Compared with the other methods, our approach achieves both a higher registration rate and better pose estimation accuracy. All methods obtain low scores on **conference-room** and **old-drinking-fountain**, likely because the thermal modality in these scenes provides weak localization cues.

Method	metallic-container					conference-room				
	AUC $\uparrow$	RRA $\uparrow$	RTA $\uparrow$	Reg (%) $\uparrow$	FPS $\uparrow$	AUC $\uparrow$	RRA $\uparrow$	RTA $\uparrow$	Reg (%) $\uparrow$	FPS $\uparrow$
COLMAP + SPSG	75.8	100.0	96.8	61.5	0.59	78.1	99.6	94.0	25.4	0.84
MA <sub>ELOFTR</sub>	14.1	97.8	43.2	50.0	0.17	2.4	56.0	9.0	15.2	0.34
MINIMA <sub>ROMA</sub>	41.0	60.7	64.6	100.0	0.04	22.5	37.3	57.6	100.0	0.04
DUST3R	23.7	75.4	54.3	100.0	0.67	15.9	34.0	43.1	100.0	0.66
MASt3R	41.2	60.9	57.3	100.0	0.27	25.6	38.0	56.8	100.0	0.26
VGGT	21.1	52.3	69.8	100.0	8.81	18.6	38.7	44.5	100.0	12.63
SEAR	67.7	95.9	91.9	100.0	8.64	46.6	74.4	71.4	100.0	11.98
Method	statue					old-drinking-fountain				
	AUC $\uparrow$	RRA $\uparrow$	RTA $\uparrow$	Reg (%) $\uparrow$	FPS $\uparrow$	AUC $\uparrow$	RRA $\uparrow$	RTA $\uparrow$	Reg (%) $\uparrow$	FPS $\uparrow$
COLMAP + SPSG	54.8	100.0	82.1	25.7	0.55	21.9	50.0	75.0	2.0	0.74
MA <sub>ELOFTR</sub>	19.7	66.8	73.6	50.5	0.11	21.1	55.9	56.9	11.7	0.12
MINIMA <sub>ROMA</sub>	58.3	76.2	75.9	100.0	0.04	49.7	60.1	61.3	100.0	0.04
DUST3R	23.4	41.8	34.5	100.0	0.67	16.8	43.2	33.6	100.0	0.67
MASt3R	35.7	49.8	57.3	100.0	0.25	37.5	45.8	52.6	100.0	0.25
VGGT	24.6	61.6	52.1	100.0	10.02	22.4	43.8	51.1	100.0	9.11
SEAR	63.1	87.6	94.0	100.0	9.81	50.9	64.7	65.6	100.0	8.92
Method	parking					telescope				
	AUC $\uparrow$	RRA $\uparrow$	RTA $\uparrow$	Reg (%) $\uparrow$	FPS $\uparrow$	AUC $\uparrow$	RRA $\uparrow$	RTA $\uparrow$	Reg (%) $\uparrow$	FPS $\uparrow$
COLMAP + SPSG	77.9	100.0	99.9	50.0	0.74	34.0	50.0	50.0	2.6	0.49
MA <sub>ELOFTR</sub>	22.4	74.5	79.5	42.8	0.15	11.4	42.8	34.7	53.6	0.12
MINIMA <sub>ROMA</sub>	44.4	48.3	53.0	100.0	0.05	62.4	100.0	98.5	100.0	0.04
DUST3R	23.0	41.9	53.6	100.0	0.67	4.8	46.2	14.2	100.0	0.68
MASt3R	45.4	49.5	57.1	100.0	0.26	44.7	78.1	58.6	100.0	0.24
VGGT	36.0	62.6	67.3	100.0	11.73	20.5	41.7	43.9	100.0	10.78
SEAR	72.1	84.3	84.5	100.0	11.45	74.8	92.7	95.0	100.0	10.55

referred to as the Jeffreys divergence). We use the KL distance because the Wasserstein distance for non-parametric distributions is computationally prohibitive due to the large number of tokens and their high dimensionality, and the Maximum Mean Discrepancy (MMD) [7] is known to be sensitive to the kernel choice. Following a procedure analogous to the Fréchet Inception Distance [11], we model the tokens of each modality as samples from multivariate Gaussian distributions and estimate the corresponding distribution parameters.

As for the experiments described in *Thermal to RGB Alignment* of the main paper, we feed a mix of RGB-thermal images to SEAR and VGGT and store the intermediate outputs of the frame-wise attention layers. We use a batch size of 12, with the thermal ratio sampled uniformly from [0.25, 0.75]. The results in Fig. 16 show the symmetrized KL divergence across layers. We observe that the divergence follows a similar trend in both models up to approximately layer 13.

**Table 11:** Per-scene metrics on the RF dataset. Our method achieves a superior registration rate and higher pose estimation accuracy than the competing methods. All methods obtain low scores on `01_Annexet_No_Radars_1` and `01_Annexet_No_Radars_2`, likely due to the complex camera motion in these sequences. In addition, the translation scores on `01_Annexet_No_Radars_3` are low because the trajectory contains frames with very small translational changes near the end, so even a slight deviation in translation can lead to large angular errors.

Method	01_Annexet_No_Radars_0									01_Annexet_No_Radars_1								
	AUC ↑	RRA ↑	RTA ↑	PCA ↓	PCC ↓	Chamfer ↓	Reg (%) ↑	FPS ↑		AUC ↑	RRA ↑	RTA ↑	PCA ↓	PCC ↓	Chamfer ↓	Reg (%) ↑	FPS ↑	
COLMAP + SPSG	58.7	100.0	76.3	3.17	1.56	2.36	49.6	0.24		86.1	100.0	99.9	1.44	1.03	1.24	24.8	0.34	
MA <sub>ELOPTR</sub>	15.4	96.6	31.5	4.27	8.47	6.37	10.3	0.12	3.8	79.1	10.4	0.68	3.05	1.87	13.9	0.16		
MINIMA <sub>ROMA</sub>	65.8	100.0	87.3	0.60	0.57	0.59	95.9	0.06	22.7	49.1	56.6	1.95	4.84	3.39	100.0	0.05		
DUS3R	21.3	48.4	33.3	0.57	10.40	5.49	100.0	0.66	14.9	27.5	49.9	1.05	6.16	3.60	100.0	0.67		
MAS3R	50.0	99.2	74.1	0.41	0.08	0.24	100.0	0.27	15.2	41.9	44.4	1.71	1.52	1.61	100.0	0.25		
VGGT	24.4	49.5	50.3	1.19	0.71	0.95	100.0	9.92	12.0	44.2	40.4	1.62	10.08	5.85	100.0	10.39		
SEAR	78.5	100.0	94.2	0.45	0.14	0.30	100.0	9.48	53.7	99.9	84.4	0.93	0.12	0.53	100.0	9.98		
Method	01_Annexet_No_Radars_2									01_Annexet_No_Radars_3								
	AUC ↑	RRA ↑	RTA ↑	PCA ↓	PCC ↓	Chamfer ↓	Reg (%) ↑	FPS ↑		AUC ↑	RRA ↑	RTA ↑	PCA ↓	PCC ↓	Chamfer ↓	Reg (%) ↑	FPS ↑	
COLMAP + SPSG	36.0	86.5	74.9	2.15	2.08	2.11	20.2	0.35	15.1	100.0	27.9	2.31	6.12	4.21	31.0	0.26		
MA <sub>ELOPTR</sub>	4.0	51.8	21.7	0.13	4.68	2.41	13.4	0.12	10.0	100.0	22.1	0.49	4.19	2.34	40.2	0.18		
MINIMA <sub>ROMA</sub>	29.4	87.6	52.7	0.76	1.18	0.97	100.0	0.05	6.7	100.0	16.1	1.20	5.18	3.19	79.9	0.05		
DUS3R	14.0	31.6	36.3	0.73	8.52	4.62	100.0	0.65	7.7	49.5	25.4	0.59	4.65	2.62	100.0	0.67		
MAS3R	28.5	95.3	53.9	0.91	0.66	0.78	100.0	0.25	16.8	100.0	37.3	0.41	3.40	1.90	100.0	0.28		
VGGT	16.9	65.7	42.6	0.77	0.69	0.73	100.0	10.19	14.3	46.9	43.1	0.68	3.64	2.16	100.0	12.05		
SEAR	63.3	99.9	89.5	0.68	0.07	0.38	100.0	9.78	51.7	100.0	78.4	0.38	0.11	0.25	100.0	11.49		
Method	04_Forest_pass_no_radars_0									04_Forest_pass_no_radars_1								
	AUC ↑	RRA ↑	RTA ↑	PCA ↓	PCC ↓	Chamfer ↓	Reg (%) ↑	FPS ↑		AUC ↑	RRA ↑	RTA ↑	PCA ↓	PCC ↓	Chamfer ↓	Reg (%) ↑	FPS ↑	
COLMAP + SPSG	96.9	100.0	100.0	1.96	0.98	1.47	50.0	0.25	96.3	100.0	99.9	0.55	0.64	0.59	50.0	0.31		
MA <sub>ELOPTR</sub>	5.3	86.3	18.1	0.41	5.01	2.71	26.9	0.12	1.6	100.0	6.6	1.49	5.23	3.36	7.3	0.14		
MINIMA <sub>ROMA</sub>	76.7	100.0	93.3	1.41	0.74	1.08	100.0	0.06	79.6	100.0	96.0	0.71	0.37	0.54	100.0	0.06		
DUS3R	23.2	49.6	61.0	1.31	1.84	1.57	100.0	0.66	20.5	49.0	44.4	0.97	2.23	1.60	100.0	0.67		
MAS3R	62.1	100.0	90.7	0.94	0.06	0.50	100.0	0.25	47.5	99.0	82.4	0.73	0.12	0.42	100.0	0.26		
VGGT	31.9	49.6	59.3	3.86	1.05	2.46	100.0	9.36	33.2	49.6	60.6	1.80	2.13	1.97	100.0	10.30		
SEAR	94.1	100.0	99.3	0.42	0.02	0.22	100.0	9.05	92.5	100.0	98.9	0.27	0.03	0.15	100.0	9.92		

After that, the divergence rises sharply for VGGT, whereas it remains low for SEAR.

## H Thermal-Only Input

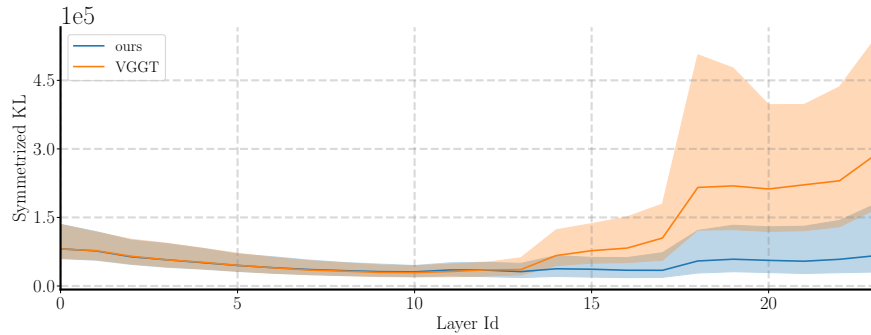
In this section, we compare the performance of VGGT and SEAR when both models are applied to thermal-only inputs. We evaluate the methods on the Public Scenes dataset, and report the results in Tab. 17. These results show that our method significantly outperforms VGGT, achieving AUC@30 of 71.8 vs 41.7, indicating that SEAR learned to process thermal images more effectively than the pre-trained VGGT model.

**Table 12:** Per-scene metrics on the ThermalGaussian dataset. Our method achieves the best pose estimation accuracy on **Ebike** and **Parterre**, while also delivering competitive performance on **Iron Ingot**.

Method	Ebike					IronIngot				
	AUC $\uparrow$	RRA $\uparrow$	RTA $\uparrow$	Reg (%) $\uparrow$	FPS $\uparrow$	AUC $\uparrow$	RRA $\uparrow$	RTA $\uparrow$	Reg (%) $\uparrow$	FPS $\uparrow$
COLMAP + SPSG	64.8	70.2	70.4	95.8	0.60	92.5	100.0	99.3	100.0	0.54
MA <sub>ELOFTR</sub>	44.6	77.8	66.7	7.3	0.38	12.8	55.9	57.4	61.5	0.12
MINIMA <sub>ROMA</sub>	93.9	100.0	100.0	100.0	0.07	94.2	100.0	99.6	100.0	0.06
DUST3R	20.0	29.7	35.9	100.0	0.65	15.6	74.9	39.9	100.0	0.66
MASt3R	90.0	100.0	99.5	100.0	0.24	73.3	100.0	96.4	100.0	0.23
VGGT	84.3	100.0	98.2	100.0	16.06	31.9	68.3	70.1	100.0	14.13
SEAR	95.2	100.0	100.0	100.0	15.07	82.1	100.0	96.4	100.0	13.34

Method	Parterre				
	AUC $\uparrow$	RRA $\uparrow$	RTA $\uparrow$	Reg (%) $\uparrow$	FPS $\uparrow$
COLMAP + SPSG	35.0	100.0	50.0	3.0	0.53
MA <sub>ELOFTR</sub>	32.1	66.4	85.5	24.2	0.23
MINIMA <sub>ROMA</sub>	33.9	47.4	64.2	100.0	0.04
DUST3R	43.2	95.3	79.5	100.0	0.65
MASt3R	85.6	100.0	98.8	100.0	0.22
VGGT	65.4	87.2	86.0	100.0	13.81
SEAR	93.7	100.0	100.0	100.0	13.01



**Fig. 16:** The blue line represents the median symmetrized KL-divergence between RGB-thermal tokens dependency across layers for SEAR method. The orange line represents the same dependency for the VGGT model. The filled area represents the boundary from 0.25– to 0.75–quantiles.

**Table 13:** Per-scene metrics on ThermalNeRF. Our method achieves a superior registration rate and higher pose estimation accuracy than the competing methods.

Method	sink					generator				
	AUC $\uparrow$	RRA $\uparrow$	RTA $\uparrow$	Reg (%) $\uparrow$	FPS $\uparrow$	AUC $\uparrow$	RRA $\uparrow$	RTA $\uparrow$	Reg (%) $\uparrow$	FPS $\uparrow$
COLMAP + SPSG	86.4	100.0	98.5	38.2	0.61	52.7	79.8	73.8	100.0	0.64
MA <sub>ELOFTR</sub>	12.4	87.2	35.0	37.3	0.24	4.2	53.1	27.0	19.7	0.22
MINIMA <sub>ROMA</sub>	48.8	100.0	70.5	100.0	0.07	62.1	100.0	84.5	100.0	0.06
DUST3R	33.6	100.0	61.6	100.0	0.67	7.4	41.4	32.9	100.0	0.66
MASt3R	58.8	100.0	85.6	100.0	0.24	32.3	84.8	47.3	100.0	0.24
VGGT	28.5	43.3	53.1	100.0	15.55	20.7	41.7	50.2	100.0	12.60
SEAR	88.1	100.0	99.5	100.0	14.42	90.9	100.0	99.1	100.0	11.99

**Table 14:** Per-scene metrics on the ThermoScenes dataset. Our method achieves a higher registration rate and better pose estimation accuracy than the competing methods. All methods achieve low scores on `freezing_ice_cup` and `melting_ice_cup`, likely due to the inherent difficulty of these scenes.

Method	freezing_ice_cup					prpt-cup				
	AUC $\uparrow$	RRA $\uparrow$	RTA $\uparrow$	Reg (%) $\uparrow$	FPS $\uparrow$	AUC $\uparrow$	RRA $\uparrow$	RTA $\uparrow$	Reg (%) $\uparrow$	FPS $\uparrow$
COLMAP + SPSG	34.5	57.2	60.5	50.0	0.52	51.4	72.0	75.3	48.1	0.61
MA <sub>ELOFTR</sub>	1.5	30.6	22.3	7.6	0.33	20.2	70.0	40.0	2.6	0.27
MINIMA <sub>ROMA</sub>	4.3	12.0	25.4	100.0	0.04	7.1	20.9	31.0	100.0	0.04
DUST3R	14.6	30.1	42.4	100.0	0.66	19.9	28.2	33.6	100.0	0.65
MASt3R	15.3	38.0	39.0	100.0	0.22	24.6	55.9	50.3	100.0	0.22
VGGT	13.2	27.2	35.9	100.0	4.89	17.6	45.9	41.4	100.0	4.09
SEAR	18.3	35.1	45.2	100.0	4.76	81.2	99.9	97.1	100.0	4.00

Method	reflect-robot					melting_ice_cup				
	AUC $\uparrow$	RRA $\uparrow$	RTA $\uparrow$	Reg (%) $\uparrow$	FPS $\uparrow$	AUC $\uparrow$	RRA $\uparrow$	RTA $\uparrow$	Reg (%) $\uparrow$	FPS $\uparrow$
COLMAP + SPSG	6.5	67.3	28.4	29.0	0.54	0.7	13.1	19.8	25.8	0.56
MA <sub>ELOFTR</sub>	15.0	80.1	41.6	11.3	0.16	3.7	28.7	20.2	8.8	0.28
MINIMA <sub>ROMA</sub>	59.0	90.0	85.4	100.0	0.04	5.5	16.9	20.3	100.0	0.03
DUST3R	13.2	37.2	28.9	100.0	0.66	19.0	39.6	40.6	100.0	0.68
MASt3R	22.8	80.7	33.1	100.0	0.24	25.6	36.8	47.0	100.0	0.24
VGGT	17.3	45.5	38.5	100.0	4.94	22.2	39.0	42.1	100.0	6.81
SEAR	63.0	94.2	88.7	100.0	4.81	37.0	50.9	59.4	100.0	6.59

Method	INR-building				
	AUC $\uparrow$	RRA $\uparrow$	RTA $\uparrow$	Reg (%) $\uparrow$	FPS $\uparrow$
COLMAP + SPSG	58.0	100.0	76.6	49.7	0.49
MA <sub>ELOFTR</sub>	8.7	73.0	37.2	15.6	0.19
MINIMA <sub>ROMA</sub>	54.3	100.0	80.6	100.0	0.03
DUST3R	27.7	94.2	55.7	100.0	0.66
MASt3R	9.0	38.0	39.3	100.0	0.25
VGGT	33.7	87.3	64.9	100.0	4.92
SEAR	82.5	100.0	95.9	100.0	4.79

**Table 15:** Per-scene metrics on the ThermalMix dataset. Our method achieves a higher registration rate and better pose estimation accuracy than the competing methods.

Method	panel					laptop				
	AUC $\uparrow$	RRA $\uparrow$	RTA $\uparrow$	Reg (%) $\uparrow$	FPS $\uparrow$	AUC $\uparrow$	RRA $\uparrow$	RTA $\uparrow$	Reg (%) $\uparrow$	FPS $\uparrow$
COLMAP + SPSG	15.8	31.8	46.4	28.0	0.32	56.1	100.0	91.6	10.8	0.28
MA <sub>ELOFTR</sub>	43.7	76.4	98.6	35.4	0.36	20.6	51.0	56.4	48.9	0.15
MINIMA <sub>ROMA</sub>	74.9	95.2	93.1	100.0	0.05	77.1	94.8	94.2	100.0	0.04
DUS <sub>t3R</sub>	15.9	70.4	39.5	100.0	0.65	21.1	44.0	45.9	100.0	0.67
MAS <sub>t3R</sub>	34.9	64.5	66.2	100.0	0.23	29.6	61.7	73.8	100.0	0.23
VGGT	13.0	28.3	44.0	100.0	17.04	15.6	30.6	41.3	100.0	11.23
SEAR	83.3	99.3	98.8	100.0	15.72	90.4	100.0	99.3	100.0	10.70

**Table 16:** Relative camera pose estimation results on METU\_VisTIR for multimodal methods. Our method outperforms all competing approaches by a large margin on nearly all metrics. The only exception is RRA@20, where it achieves a result slightly higher than that of MINIMA<sub>ROMA</sub>.

Method	AUC@5 $\uparrow$	AUC@10 $\uparrow$	AUC@20 $\uparrow$	RRA@5 $\uparrow$	RRA@10 $\uparrow$	RRA@20 $\uparrow$	RTA@5 $\uparrow$	RTA@10 $\uparrow$	RTA@20 $\uparrow$
MA <sub>ELOFTR</sub>	0.3	1.0	4.5	7.1	17.8	37.3	3.0	8.1	23.6
MINIMA <sub>ROMA</sub>	9.4	27.2	50.9	62.7	88.6	98.0	37.1	63.9	84.7
VGGT	1.8	8.2	21.9	60.4	76.2	84.9	7.4	24.6	47.6
SEAR	23.6	47.3	68.0	92.3	97.5	98.1	57.7	81.9	92.8

**Table 17:** Results on the Public Scenes dataset using only thermal modality. The table compares SEAR and VGGT when only thermal images are passed to the networks.

Method	AUC@30 $\uparrow$	RRA@30 $\uparrow$	RTA@30 $\uparrow$	PCA $\downarrow$	PCC $\downarrow$	Chamfer $\downarrow$
VGGT	41.7	75.8	67.9	0.96	0.20	0.58
SEAR	71.8	93.7	90.8	0.49	0.07	0.28